Ore Geology Reviews 88 (2017) 270–288

Contents lists available at ScienceDirect

Ore Geology Reviews

journal homepage: www.elsevier.com/locate/oregeo

Magmatism and metallogenic mechanisms of the Baoshan Cu-polymetallic deposit from the Lesser Xing'an Range, NE China: Constraints from geology, geochronology, geochemistry, and Hf isotopes

Liang Ren [a], Jinggui Sun [a,*], Jilong Han [a], Yang Liu [a], Changsheng Wang [b], Alei Gu [c], Keqiang Zhao [a], Ridong Yu [a]

[a] College of Earth Sciences, Jilin University, Changchun 130061, China
[b] Team 707, Heilongjiang Bureau of Geological Exploration for Nonferrous Metals, Suihua 152000, China
[c] Tianjin Center of China Geological Survey, Tianjin 300170, China

ARTICLE INFO

Article history:
Received 7 November 2016
Received in revised form 9 May 2017
Accepted 10 May 2017
Available online 13 May 2017

Keywords:
Zircon U–Pb dating
Molybdenite Re–Os dating
Geochemistry
Hf isotope
Baoshan skarn Cu–polymetallic deposit
Lesser Xing'an Range

ABSTRACT

The Baoshan Cu-polymetallic deposit is a recently discovered skarn deposit in the northern Lesser Xing'an Range, NE China. The orebodies are mainly hosted in the contact zone between granitic intrusions and Lower Cambrian dolomitic crystalline limestones or skarns. We present here zircon U–Pb and molybdenite Re–Os age data, whole-rock geochemistry, and zircon Hf isotopic data to constrain the geodynamic mechanisms of igneous activity and metallogenesis within the Baoshan Cu–polymetallic deposit. LA–ICP–MS zircon U–Pb dating suggests that a hornblende–quartz monzonite and porphyritic biotite granite were emplaced at 252.45 ± 0.70 Ma and 251.10 ± 0.98 Ma, respectively. Molybdenite separated from ore-bearing quartz veins or skarn-type ores yields a weighted mean model age of 250.3 ± 3.4 Ma, which coincide with the emplacement of the igneous rocks. These data suggest that the Late Permian-Early Triassic magmatic and mineralization event led to the formation of the Baoshan Cu–polymetallic deposit. Granitic intrusions are closely associated with this mineralization and have high contents of SiO_2 (60.90–68.98 wt.%), Al_2O_3 (15.15–16.98 wt.%) and K_2O (2.77–4.17 wt.%), with A/CNK ratios of 0.86–0.96. These granites are classified as metaluminous and high-K calc-alkaline I-type granites, and are enriched in Rb, Th, U, and K, and depleted in Nb, Ta, P, and Ti. Moreover, Moreover, the hornblende–quartz monzonite and porphyritic biotite granite have geochemical characteristics similar to adakites and island arc calc-alkaline rocks, respectively. In situ zircon Hf isotope data on the hornblende–quartz monzonite samples show $\varepsilon_{Hf}(t)$ values from +0.1 to +3.1, and porphyritic biotite granite samples exhibit heterogeneous $\varepsilon_{Hf}(t)$ values from −5.4 to +1.1. The geochemical and isotopic data for the Baoshan intrusions indicate that the Late Permian–Early Triassic continental–continental collision caused over thickening and delamination of the lower crust. Partial melting of delaminated lower crust formed the primary adakitic magmas, which may have reacted with surrounding mantle peridotite during ascent. Hornblende–quartz monzonite was formed by the emplacement of the adakitic magmas, whereas the formation of the porphyritic biotite granite was caused by the mixing of adakitic magmas with ancient crustal materials during ascent. Moreover, ore-forming materials were typically derived from the adakitic magmas with high oxygen fugacity, which incorporated significant amounts of ore-forming elements. Based on the regional geological history and the new geochemical and isotopic data from intrusions, we suggest that diagenesis and mineralization of the Baoshan Cu–polymetallic deposit took place in a transitional tectonic setting from collisional orogeny to extension, after collision of the North China Plate and Songnen Block, during the latter stages of the Xingmeng orogeny.

1. Introduction

The Lesser Xing'an Range is located in the eastern segment of the Central Asian Orogenic Belt (CAOB; Fig. 1A, B), a complex tectonic region formed during the evolution of the Paleo-Asian Ocean,

* Corresponding author at: 2199 Jianshe Street, College of Earth Sciences, Jilin University, Changchun 130061, PR China.
E-mail address: sunjinggui@jlu.edu.cn (J. Sun).

http://dx.doi.org/10.1016/j.oregeorev.2017.05.009
0169-1368/

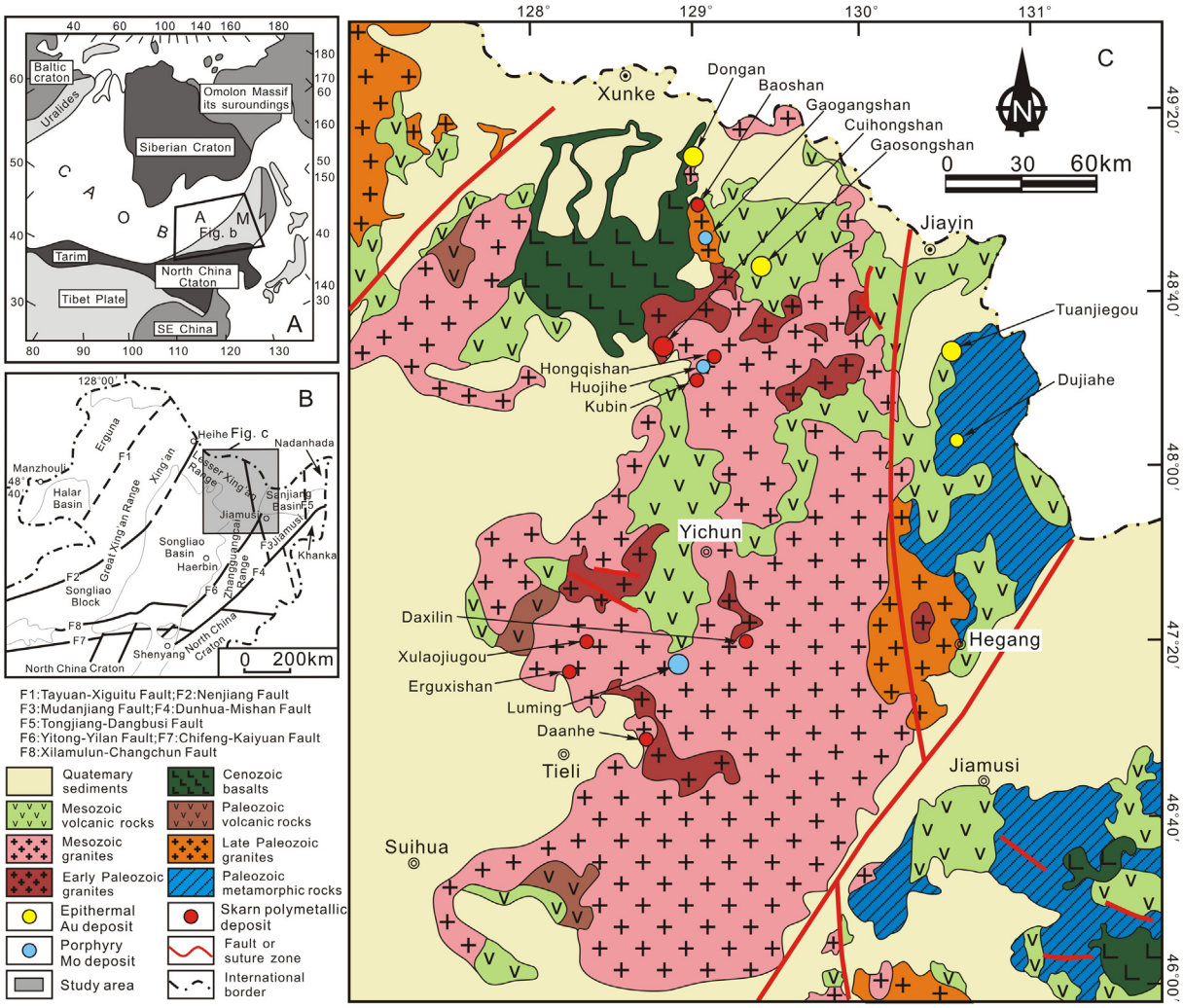

Fig. 1. (A) Location of Northeast China with respect to the main tectonic units of China and Russia, modified after Wu et al. (2007a). 'A' and 'M' represent the Altaids and Manchrids. (B) Tectonic sketch maps of Northeast China, modified after Shao and Tang (1995), Wu et al. (2000). (C) Simplified geological map of the Lesser Xing'an range, modified after Zhang et al. (2010), Wu et al. (2011), Cui et al. (2013).

closure of the Mongol–Okhotsk Ocean, and subduction of the Pacific Plate, as well as Cenozoic supercrustal faulting (Scedilengör et al., 1993; Jahn et al., 2000, 2004; Windley et al., 2007; Zhang et al., 2008, 2009; Wu et al., 2011; Zhou et al., 2011a,b; Xu et al., 2012). The multi–phase tectonic, magmatic, sedimentary, and metamorphic events resulted in the Lesser Xing'an Range, which is characterized by Paleozoic metamorphic rocks, late Mesozoic continental intermediate–felsic volcanic rocks, Paleogene fluvial and lacustrine clastic sedimentary rocks, and Phanerozoic granitic plutons. These rocks are associated with banded iron formation (BIF) ores, porphyry Mo, skarn Fe–polymetallic, and epithermal Au deposits (Fig. 1C). Recent geochronological studies indicate that the BIF deposits (e.g., Dongfengshan) formed in the late Paleozoic (288–271 Ma; Wang et al., 2014), porphyry Mo deposits (e.g., Luming and Huojihe) in the Early–Middle Jurassic (187–174 Ma; Tan et al., 2012; Liu et al., 2014; Sun et al., 2014; Hu et al., 2014a; Zhang et al., 2014; Du and Zhang, 2015), epithermal Au deposits (e.g., Dongan, Tuanjiegou, and Gaosongshan) in the Early Cretaceous (115–99 Ma; Zhang et al., 2010; Sun et al., 2013a,b; Hao et al., 2016; Liu et al., 2015), and skarn Fe–polymetallic deposits (e.g., Cuihongshan, Erguxishan, and Xulaojiugou) in the Early Jurassic (202–182 Ma; Shao et al., 2011; Hao et al., 2013; Hu et al., 2014a,b; Liang, 2014).

The Baoshan Cu–polymetallic deposit is a recently discovered small-scale skarn deposit, dominated by copper mineralization, and located in the northern Lesser Xing'an Range, NE China. However, the skarn deposits in the Lesser Xing'an Range are characterized by having iron, zinc, and lead, associated with molybdenum, tungsten, and copper. This gives rise to a number of questions, such as why copper is the main ore element of the Baoshan deposit, the mode of petrogenesis of the ores and host rocks, whether the mineralization age of the Baoshan deposit is consistent with other skarn deposits in the Lesser Xing'an Range, and the prospecting potential of the Baoshan deposit. To address these questions, we present new LA–ICP–MS zircon U–Pb and molybdenite Re–Os age data, whole-rock geochemical data, and in situ zircon Hf isotopic compositions of the Baoshan deposit. On this basis, we discuss the possible magmatic source of the intrusions and the timing of mineralization. Furthermore, these new data can be used to constrain the geodynamic setting and regional metallogenic regimes.

2. Geological background

The study area is located in the northern Lesser Xing'an Range, which straddles the Xing'an Block to the northwest and the Jiamusi

Block to the east, and is separated from these blocks by the Hegenshan–Heihe and Jiayin–Mudanjiang faults, respectively (Fig. 1C). The stratigraphy of this region is dominated by Early Cambrian marine clastic–carbonate rocks, Ordovician continental volcanic–sedimentary units, Permian terrigenous clastic–carbonate formations, Cretaceous continental intermediate–felsic volcanic rocks, and Paleogene fluvial and lacustrine clastic sedimentary rocks (HBGMR, 1993; Han et al., 1995). The Cambrian strata host numerous medium- to large-sized skarn-type deposits (Zhao, 2009), and the Cretaceous continental intermediate–felsic volcanic rocks are closely associated with epithermal Au deposits (Zhang et al., 2010; Sun et al., 2013a,b). The Lesser Xing'an Range is also characterized by widespread plutonic rocks, which are distributed along a N–S trending belt. When considered with the reported isotopic age data, the intrusive magmatism can be divided into five stages: (1) Middle Cambrian–Late Ordovician (508–450 Ma; Liu et al., 2008; Wang et al., 2016); (2) Middle–Late Permian (266–252 Ma; Wei, 2012; Yu et al., 2013); (3) Early–Middle Triassic (244–231 Ma; Wei, 2012; Ren et al., 2015); (4) Late Triassic (222–200 Ma; Sun et al., 2004a; Wu et al., 2011; Wei, 2012); and (5) Early Jurassic (186–175 Ma; Yu et al., 2012; Xu et al., 2013). Late Triassic and Early Jurassic granites are widespread and closely associated with porphyry and skarn deposits in the Lesser Xing'an Range. The structure of the region is dominated by faults striking NNE, NE, and approximately EW. The faults striking NNE and NE pre-date the EW trending, and controlled the distribution of igneous rocks and ore deposits.

3. Ore deposit geology

The Baoshan Cu–polymetallic deposit is hosted within the contact zone between the Kuerbin sag and Baoshan uplift zone in the Wudihe graben-hosted volcanic–sedimentary basin (Fig. 1C). The exposed strata in the mining area are typically of the Lower Cambrian Qianshan Formation, which consists predominantly of dolomitic crystalline limestones, sandstones, siltstones, and slates (Fig. 2). Mesozoic and Cenozoic strata are scattered and small in volume, including Early Cretaceous Jiufengshanzu Formation coal-bearing strata, Ningyuancun Formation continental intermediate–felsic volcanic rocks, Ganhe Formation continental mafic volcanic rocks, Paleocene Sunwu Formation fluvial and lacustrine clastic sedimentary rocks, and Quaternary alluvial sediments. Intermediate–felsic intrusive rocks are relatively widespread in the mining area, which was formed by two episodes of magmatism. The Middle Ordovician gneissic granite mainly distributed as bathliths, covering an area of about 4.5 km^2 in the northwest of the mining area. The Late Permian–Early Triassic granites are distributed in the southeast part of the mining area, consisting of hornblende–quartz monzonite, porphyritic biotite granite and granite aplite. Among these, the hornblende–quartz monzonite is spatially associated with the skarn and mineralization (Fig. 2), which is considered as the causative intrusion of the mineralization, and the skarn-type orebodies mainly occur in the contact between the Qianshan Formation and hornblende–quartz monzonite. In addition, a small amount of porphyritic biotite granite intruded the hornblende–quartz monzonite, mainly as stocks and dikes. In the mining area, the hornblende–quartz monzonite and porphyritic biotite granite generally exhibit a low degree of alteration. The extent of mineralization in the mining area is constrained by NE-trending secondary fractures of Atinghe Fault.

A total of 31 orebodies have been explored. These orebodies are typically hosted in the contact zone between the hornblende–quartz monzonite and the dolomitic crystalline limestones or skarns (Fig. 2), and minor non-economic Mo orebodies (considered as porphyry-type) are found in the porphyritic biotite granite within deep drill core. The skarn-type Cu mineralization extends down-dip for more than 250 m below the surface, and minor porphyry-type Mo mineralization occur with porphyritic biotite granite at ca. 400 m below the surface. The main skarn-type orebodies are stratoid, lenticular, and veined, and they are controlled by stratigraphic and lithological contacts. The main skarn-type orebodies are 100–700 m long, 2–8 m thick, and generally NE–trending and NW dipping (at 45°–70°; Fig. 2A). The ore structures are typically massive and disseminated, with some also being stockwork and banding. The ore minerals are dominated by chalcopyrite (Fig. 4E), pyrite, magnetite (Fig. 4G), molybdenite (Fig. 4F), pyrrhotite (Fig. 4H), and sphalerite (Fig. 4I), with minor bornite, chalcocite (Fig. 4E), scheelite, galena, and malachite. The gangue minerals consist of garnet (Fig. 4A, B), diopside (Fig. 4C), epidote (Fig. 4D), quartz, and calcite, with minor chlorite (Fig. 4D), tremolite, phlogopite, and actinolite. Wall-rock alteration typically occurred by skarnization, silicification, epidotization, chloritization, and carbonation. Skarn alteration is the most widely distributed, and is found along the contact zone between the hornblende–quartz monzonite and the dolomitic crystalline limestones. Ore-forming processes can be divided into five stages, according to cross-cutting relationships and mineral assemblages: (I) a prograde skarn stage; (II) a retrograde skarn stage; (III) an oxide stage; (IV) a quartz–sulfide stage; and (V) a carbonate stage. Stage I was characterized by the formation of abundant garnet, pyroxene, and wollastonite. Stage II was marked by the formation of epidote, chlorite, tremolite, actinolite, and minor quartz, together with significant amounts of magnetite mineralization, replacing the anhydrous silicate minerals of stage I. Stage III was dominated by magnetite, with lesser amounts of scheelite, chalcopyrite, and pyrrhotite. Stage IV was characterized by the precipitation of large amounts of sulfides (e.g., chalcopyrite, molybdenite, pyrrhotite, pyrite, and minor sphalerite) along with gangue minerals (e.g., quartz and chlorite), and it represents the main ore-forming stage. Carbonate veins were typically formed during stage V, but it was also associated with minor pyrite and sphalerite formation.

4. Samples and analytical methods

4.1. Samples and petrography

A hornblende–quartz monzonite sample (BZ23-1) was chosen from a depth of ~146 m in the drill core zk23-10 for zircon U–Pb dating and in situ Hf isotopic analysis. A porphyritic biotite granite sample (BZ23-2) was collected from a depth of 323 m in the drill core zk23-10 for zircon U–Pb dating and in situ Hf isotopic analysis. Four hornblende–quartz monzonite samples and six porphyritic biotite granite samples were collected from drill cores zk23-10 and zk15-10, for major and trace element analyses. A total of five molybdenite samples were selected for Re–Os analyses, collected from the drill core zk23-10 and zk15-10, and molybdenite was identified in quartz veins or as disseminated in the skarn–type ores with associated pyrite (Fig. 4F).

The hornblende–quartz monzonite is dark–gray in colour, with a medium–coarse–grained granitic texture, and a massive structure (Fig. 3A, B). The main rock–forming minerals are K–feldspar (35–40%), plagioclase (20–25%), quartz (15–20%), hornblende (10–15%) and biotite (~5%), with accessory magnetite, zircon, titanite and apatite.

The porphyritic biotite granite are off–white–light pink in colour, and has a fine– to medium–grained porphyritic texture that is defined by 45–50% phenocrysts. Phenocrysts are composed of K–feldspar (35%–40%), plagioclase (30–35%), biotite (10–15%), and hornblende (~5%). The groundmass is dominated by quartz, K–feldspar and plagioclase. The porphyritic biotite granite also

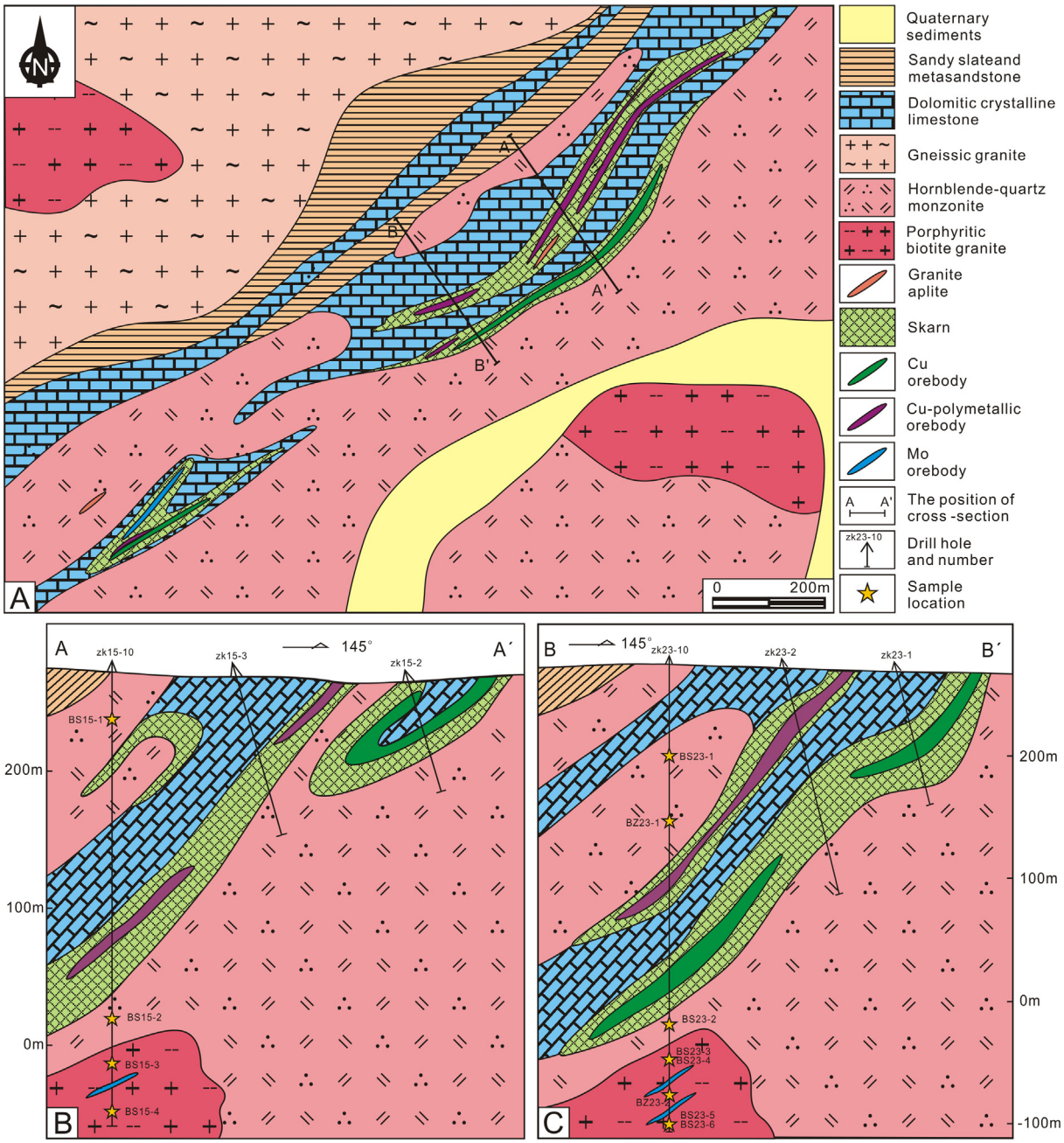

Fig. 2. (A) Simplified geological map of the Baoshan Cu–polymetallic deposit; (B) Cross–section of the Baoshan Cu–polymetallic deposit.

contains accessory magnetite, zircon and apatite (Fig. 3C, D). Some samples preserve evidence of silicification, sericitic or potassium alteration.

4.2. Zircon U–Pb dating

Zircons were extracted from the hornblende quartz monzonite (BZ23-1) and the porphyritic biotite granite (BZ23-2) using standard densityand magnetic separation techniques followed by handpicking using a binocular microscope at the Langfang Regional Geological Survey, Hebei Province, China. Lots of zircons were handpicked from each sample, and pasted on the resin disc under the binocular microscope, and then polished to expose the grain centres. Cathodoluminescence (CL) images of the zircon grains were taken using a Mono CL3 detector (manufactured by Gatan, USA) attached to a scanning electron microscope (manufactured by JSM6510, JEOL, Japan) at the Beijing Geoanalysis Co., Ltd. These images helped select suitable spots for in-situ U–Pb dating and Lu–Hf analysis.

Zircon U–Pb dating from the sample BZ23-1 was performed on an Agilient 7500c ICP–MS instrument coupled with a 193–nm ArF Excimer laser with an automatic positioning system at the Key Laboratory of Orogenic Belts and Crustal Evolution, Peking University, Beijing, China. Zircon U–Pb dating from the sample BZ23-2 were carried out using an Agilient 7900 ICP–MS instrument coupled with a 193-nm ArF Excimer laser (COMPexPro 102, Coherent, DE) with the automatic positioning system at MLR Key laboratory of Mineral Resources Evaluation in Northeast Asia, Jilin University, Changchun, China. Detailed analytical procedure of the two labs were basically the same. During analysis, laser spot size was set

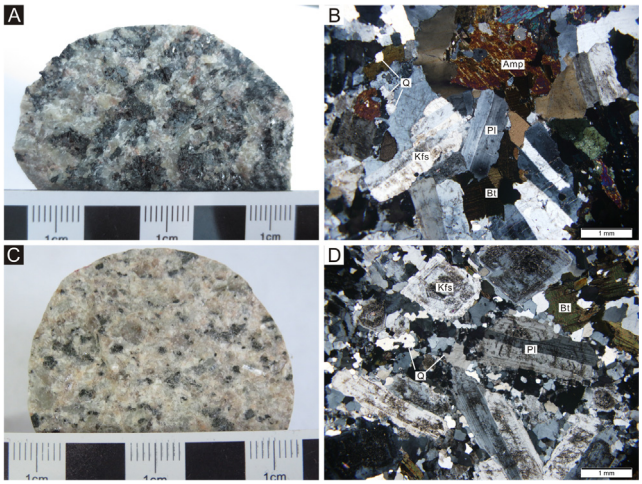

Fig. 3. Hand specimen photographs (A, C) and thin section photomicrographs (B, D; cross–polarized light) of hornblende–quartz monzonite and the porphyritic biotite granite of the Baoshan Cu–polymetallic deposit. Abbreviations: Bt = biotite; Kfs = K–feldspar; Pl = plagioclase; Q = quartz.

to 32 μm for most analyses, laser energy density at 10 J/cm^2 and repetition rate at 8 Hz, with data acquired over a duration of 80–120 s. Calibrations for elemental concentration analysis in zircon were performed using NIST 610 glass as an external standard and ^{29}Si as internal standard. U–Pb isotope fractionation effects were corrected using zircon Plesovice (337 Ma) as external standard. Zircon standard 91,500 was used as a secondary standard to supervise the deviation of age measurement/calculation. Isotopic ratios and element concentrations of zircons were calculated using software GLITTER (ver. 4.4.2, Macquarie University). Concordia diagrams were constructed using Isoplot/Ex (3.0) (Ludwig, 2003). Common lead was corrected using LA–ICP–MS Common Lead Correction (ver. 3.15), following the method of Andersen (2002). The analytical data are presented on U–Pb Concordia diagrams with 2σ errors. The mean ages are weighted means at 95% confidence levels (Ludwig, 2003).

4.3. Molybdenite Re–Os dating

Five samples of molybdenite were collected for Re–Os dating from the Baoshan Cu–polymetallic deposit. Gravity and magnetic separation techniques were applied to crushed samples, and molybdenite grains were handpicked under a binocular microscope (purity > 99%). Re–Os isotope analyses were performed using a inductively coupled plasma mass spectrometer (ICP–MS) at the State Key Laboratory of Isotope Geochemistry, Guangzhou Institute of Geochemistry, Chinese Academy of Sciences, China. The Carius tubes method was used to digest sample (Shirey and Walker, 1995), and Re and Os were separated using the distillation technique described in Du et al. (2004). Details of the chemical procedure were described by Sun et al. (2001, 2010). The average blanks for Re and Os are 2.8 pg and 0.7 pg, respectively. These blanks have negligible effect on the measured Re and Os abundances. The analytical reliability was tested by repeated analyses of the molybdenite standard HLP–5, which is a carbonate rock vein–type molybdenum–lead deposit in the Jingduicheng–Huanglongpu area of shanxi Province, China (Sun et al., 2001, 2010). The uncertainty

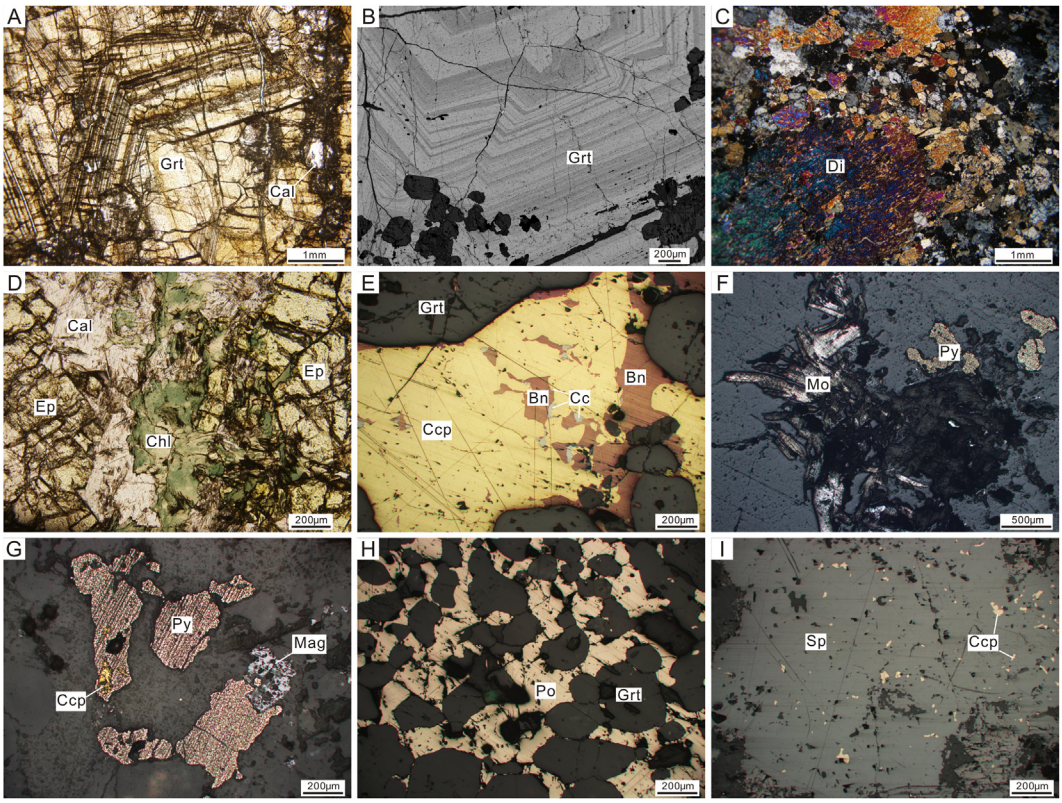

Fig. 4. Photographs of skarn and mineralization features in the Baoshan Cu–polymetallic deposit. (A) a typical oscillatory zoned garnet crystal; (B) back–scattered electron (BSE) image showing typical oscillatory zoned garnet; (C) tabular and granular diopside crystals show simple twins and clustered twins; (D) calcite replaced by epidote and chlorite; (E) chalcopyrite replaced by bornite and chalcocite; (F) microscopic picture of paragenetic pyrite and molybdenite; (G) mineral assemblage consisting of pyrite, chalcopyrite and magnetite; (H) garnet replected by pyrrhotite; (I) chalcopyrite developed in sphalerite as exsolution lamellae; Abbreviations: Grt = garnet; Di = diopside; Ep = epidote; Chl = chlorite; Cal = calcite; Ccp = chalcopyrite; Py = pyrite; Bn = bornite; Cc = chalcocite; Mo = molybdenite; Po = pyrrhotite; Sp = sphalerite.

Table 1
LA-ICP-MS zircon U-Pb data of hornblende–quartz monzonite (BZ23–1) and porphyritic biotite granite (BZ23–2) from the Baoshan Cu-polymetallic deposit.

Spot	Element (ppm)		Th/U	Isotope ratio	Apparent age (Ma)											
	P b *	Th	U		$^{207}Pb/^{206}Pb$	1σ	$^{207}Pb/^{235}U$	1σ	$^{206}Pb/^{238}U$	1σ	$^{207}Pb/^{206}Pb$	1σ	$^{207}Pb/^{235}U$	1σ	$^{206}Pb/^{238}U$	1σ
BZ23-1, hornblende–quartz monzonite, 23 spots, weighted mean age = 252.45 ± 0.70 Ma, MSWD = 0.17																
BZ23-1-01	7	94	129	0.73	0.05135	0.00223	0.28313	0.01192	0.03998	0.00054	257	97	253	9	253	3
BZ23-1-02	7	131	138	0.95	0.05191	0.00330	0.28338	0.01748	0.03959	0.00072	282	139	253	14	250	4
BZ23-1-03	7	158	138	1.15	0.05165	0.00339	0.28279	0.01804	0.03971	0.00074	270	144	253	14	251	5
BZ23-1-04	8	150	155	0.97	0.05196	0.00453	0.28662	0.02424	0.04000	0.00100	284	187	256	19	253	6
BZ23-1-05	4	44	73	0.61	0.05105	0.00394	0.28252	0.02125	0.04013	0.00084	243	169	253	17	254	5
BZ23-1-06	10	137	193	0.71	0.05167	0.00183	0.28415	0.00971	0.03988	0.00049	271	79	254	8	252	3
BZ23-1-07	15	233	281	0.83	0.05124	0.00206	0.28373	0.01099	0.04016	0.00055	252	90	254	9	254	3
BZ23-1-08	9	143	168	0.85	0.05137	0.00212	0.28307	0.01131	0.03996	0.00053	258	92	253	9	253	3
BZ23-1-09	8	136	163	0.84	0.05133	0.00238	0.28242	0.01268	0.03990	0.00057	256	103	253	10	252	4
BZ23-1-10	7	128	138	0.93	0.05164	0.00250	0.28413	0.01330	0.03991	0.00061	269	107	254	11	252	4
BZ23-1-11	9	156	171	0.91	0.05124	0.00243	0.28132	0.01295	0.03982	0.00059	252	106	252	10	252	4
BZ23-1-12	8	146	156	0.93	0.05126	0.00348	0.28265	0.01863	0.03999	0.00080	253	149	253	15	253	5
BZ23-1-13	10	124	199	0.62	0.05156	0.00388	0.28311	0.02060	0.03982	0.00089	266	164	253	16	252	6
BZ23-1-14	10	173	184	0.94	0.05122	0.00210	0.28304	0.01124	0.04007	0.00054	251	92	253	9	253	3
BZ23-1-15	7	127	141	0.90	0.05112	0.00237	0.28057	0.01265	0.03981	0.00055	246	103	251	10	252	3
BZ23-1-16	7	114	128	0.89	0.05101	0.00196	0.28064	0.01047	0.03990	0.00048	241	86	251	8	252	3
BZ23-1-17	24	374	482	0.78	0.05098	0.00131	0.28126	0.00691	0.04001	0.00043	240	58	252	5	253	3
BZ23-1-18	8	102	174	0.59	0.05120	0.00170	0.28296	0.00913	0.04008	0.00045	250	75	253	7	253	3
BZ23-1-19	7	122	141	0.86	0.05154	0.00274	0.28347	0.01469	0.03989	0.00059	265	117	253	12	252	4
BZ23-1-20	7	96	135	0.72	0.05094	0.00182	0.28068	0.00974	0.03996	0.00046	238	80	251	8	253	3
BZ23-1-21	6	80	118	0.68	0.05134	0.00190	0.28223	0.01012	0.03987	0.00048	256	83	252	8	252	3
BZ23-1-22	5	65	98	0.66	0.05116	0.00302	0.28124	0.01616	0.03987	0.00065	248	130	252	13	252	4
BZ23-1-23	29	457	579	0.79	0.05113	0.00090	0.28188	0.00464	0.03998	0.00038	247	40	252	4	253	2
BZ23-2, porphyritic biotite granite, 15 spots, weighted mean age = 251.10 ± 0.98 Ma, MSWD = 0.25																
BZ23-2-01	6	66	107	0.62	0.05130	0.00314	0.28137	0.01652	0.03977	0.00086	255	135	252	13	251	5
BZ23-2-02	4	41	74	0.56	0.05121	0.00200	0.28144	0.01063	0.03985	0.00062	250	87	252	8	252	4
BZ23-2-03	7	144	114	1.27	0.05167	0.00170	0.28307	0.00902	0.03973	0.00057	271	74	253	7	251	4
BZ23-2-04	4	42	73	0.58	0.05129	0.00321	0.28153	0.01689	0.03981	0.00087	254	138	252	13	252	5
BZ23-2-05	4	50	73	0.68	0.05111	0.00265	0.28007	0.01396	0.03975	0.00076	246	115	251	11	251	5
BZ23-2-06	9	149	183	0.81	0.05181	0.00215	0.28019	0.01118	0.03922	0.00065	277	92	251	9	248	4
BZ23-2-07	5	73	107	0.68	0.05130	0.00301	0.28110	0.01579	0.03974	0.00083	255	129	252	13	251	5
BZ23-2-08	30	607	489	1.24	0.05202	0.00108	0.28502	0.00578	0.03974	0.00048	286	47	255	5	251	3
BZ23-2-09	19	351	324	1.08	0.05126	0.00103	0.28069	0.00556	0.03971	0.00048	253	46	251	4	251	3
BZ23-2-10	5	72	99	0.73	0.05136	0.00208	0.28088	0.01092	0.03967	0.00065	257	90	251	9	251	4
BZ23-2-11	6	86	117	0.74	0.05201	0.00351	0.28262	0.01826	0.03941	0.00094	286	147	253	14	249	6
BZ23-2-12	34	504	639	0.79	0.05096	0.00095	0.28013	0.00514	0.03987	0.00047	239	42	251	4	252	3
BZ23-2-13	3	37	58	0.65	0.05147	0.00319	0.28212	0.01676	0.03975	0.00087	262	136	252	13	251	5
BZ23-2-14	5	58	94	0.61	0.05125	0.00155	0.28067	0.00823	0.03972	0.00055	252	68	251	7	251	3
BZ23-2-15	5	69	101	0.68	0.05092	0.00153	0.27940	0.00811	0.03979	0.00055	237	68	250	6	252	3

Table 2
Molybdenite Re-Os isotopic data for the Baoshan Cu-polymetallic deposit.

Sample	Weight/g	Re/μg g^{-1}		^{187}Re/μg g^{-1}		^{187}Os/ng/g		Age/Ma	
		Content	2σ	Content	2σ	Content	2σ	Model T	2σ
BS-1	0.0706	6.292	0.057	3.955	0.036	16.203	0.086	245.43	2.56
BS-2	0.0717	5.483	0.052	3.446	0.033	14.457	0.058	251.26	2.59
BS-3	0.0715	5.092	0.045	3.200	0.029	13.417	0.098	251.10	2.89
BS-4	0.0706	5.976	0.046	3.756	0.029	15.973	0.082	254.70	2.36
BS-5	0.0207	4.929	0.024	3.098	0.015	12.922	0.006	249.85	1.23

in each individual age determination was about 0.35% including the uncertainty of the decay constant of ^{187}Re, uncertainty in isotope ratio measurement, and spike calibrations. The average Re–Os age for HLP–5 is 221.3 ± 0.3 Ma with confidence limit of 95% (Stein et al., 1997). Median age and mean absolute deviation were 221.34 ± 0.12 Ma. The average Re concentration was 283.71 ± 1.54 ppb. The average Os concentration was 657.95 ± 4.74 ppb. Molybdenite model ages were calculated using a ^{187}Re decay constant of 1.666×10^{-11} per year (Smoliar et al., 1996), following the equation $t = [\ln(1 + {}^{187}Os/{}^{187}Re)]/\lambda$, where λ is the decay constant of ^{187}Re. The results of Re–Os dating of molybdenite samples are summarized in Table 2.

4.4. Major and trace element determinations

Prior to geochemical and isotopic analysis, sample were cleaned of altered surfaces and were crushed in an agate mill to a powder (~200 diameter mesh) at the Langfang Regional Geological Survey, Hebei Province, China. Major element analyses were determined by XRF with analytical uncertainties ranging from 1% to 3%. Trace element compositions were determined using an Agilent 7500a inductively coupled plasma mass spectrometer (ICP–MS), with detailed analytical procedures described in Gao et al. (2002). The major and trace element compositions of intermediate–felsic intrusive rocks associated with the Baoshan Cu–polymetallic deposit are given in Table 3.

4.5. Zircon Lu–Hf isotope analyses

Zircon Lu–Hf isotope analyses were conducted using a New Wave UP193FX laser ablation microprobe attached to a Neptune multi–collector ICP–MS in the State Key Laboratory for Mineral Deposits Research at Nanjing University. The instrumental conditions and data acquisition were similar to those described by Wu et al. (2006) and Hou et al. (2007). Analyses were performed predominantly with a beam diameter of 35 μm anda repetition rate of 8 Hz. Both He and Ar carrier gases were used to transport the ablated sample from the laser–ablation cell via a mixing chamber to the ICP–MS torch. Atomic masses 172, 173, 175 to 180 and 182 were simultaneously measured in the static–collection mode. Corrections for isobaric interferences of ^{176}Yb and ^{176}Lu on ^{176}Hf referred to Iizuka and Hirata (2005), Wu et al. (2006), and Hou et al. (2007). The reference zircon Mud Tank ($^{176}Hf/^{177}Hf = 0.282507 \pm 6$; Woodhead and Hergt, 2005) and the standard zircon 91500 were used to monitor performance conditions and analytical accuracy. The initial Hf values (in term of ε_{Hf}) were calculated using a decay constant of 1.865×10^{-11} per year (Scherer et al., 2001) for ^{176}Lu and a chondritic model with $^{176}Hf/^{177}Hf = 0.282772$ and $^{176}Lu/^{177}Hf = 0.0332$ (Blichert–Toft and Albarède, 1997). Depleted mantle Hf model ages (T_{DM}) were calculated using the measured $^{176}Lu/^{177}Hf$ ratios of zircon, referring to a model of depleted mantle with a present–day $^{176}Hf/^{177}Hf$ ratio of 0.28325, similar to that of an average MORB (Nowell et al., 1998) and $^{176}Lu/^{177}Hf = 0.0384$ (Griffin et al., 2000), and an average crust f_{CC} ratio of −0.55 (Griffin et al., 2002). All Lu–Hf isotope results are reported with 2σ uncertainties, and the results of the zircon Hf isotope analyses undertaken during this are given in Table 4.

5. Results

5.1. Zircon U–Pb dating

The Baoshan hornblende–quartz monzonite (BZ23-1) and porphyritic biotite granite (BZ23-2) were selected for LA–ICP–MS zircon U–Pb dating (Table 1). Zircon grains are typically euhedral–subhedral, prismatic (50–200 μm long), and show aspect ratio of 3:2 to 3:1. Zircons exhibit clear oscillatory growth zoning in CL images (Fig. 5), with varying concentrations of U (58–639 ppm) and Th (37–607 ppm), and Th/U ratios from 0.23 to 1.27, indicating a magmatic origin (Koschek, 1993; Hoskin and Schaltegger, 2003). All analytical results plot near the concordia line (Fig. 6). Zircon grains collected from the hornblende–quartz monzonite (BZ23-1) yielded $^{206}Pb/^{238}U$ ages of 250–254 Ma, with a weighted mean $^{206}Pb/^{238}U$ age of 252.45 ± 0.70 Ma (n = 23), and a mean squared weighted deviation (MSWD) of 0.17 (Fig. 6A). Zircon grains collected from the porphyritic biotite granite (BZ23-2) yielded $^{206}Pb/^{238}U$ ages of 248–252 Ma, with a weighted mean $^{206}Pb/^{238}U$ age of 251.10 ± 0.98 Ma (n = 15) and MSWD of 0.25 (Fig. 6B). We therefore interpret the two weighted mean ages as representing the emplacement ages of the hornblende–quartz monzonite and porphyritic biotite granite.

5.2. Molybdenite Re–Os isotopic ages

The Re–Os isotopic data for five molybdenite samples from the Baoshan Cu–polymetallic deposit are listed in Table 2 and plotted in an isochron diagram in Fig. 7. The concentrations of ^{187}Re and ^{187}Os ranged from 3.10 to 3.96 μg/g and from 12.92 to 16.20 ng/g, respectively. Five samples yielded model ages of 245.43 ± 2.56 to 254.70 ± 2.36 Ma, with a well-defined ^{187}Re–^{187}Os isochron age of 245 ± 61 Ma (MSWD = 2.5) and an initial ^{187}Os of 0.3 ± 3.5 ng/g (Fig. 7A). The data also yield a weighted mean model age of 250.3 ± 3.4 Ma (MSWD = 7.4; Fig. 7B). Because of the large error in the isochron age, the weighted mean model age has been used to infer the timing of molybdenite mineralization. This model age also suggests that the Baoshan Cu–polymetallic deposit was mineralized during the Late Permian to Early Triassic.

5.3. Whole-rock geochemistry

The representative whole-rock geochemical data for the Baoshan intrusive samples are presented in Table 3. The hornblende–quartz monzonites contain 60.90–63.03 wt.% SiO_2, 16.06–16.38 wt.% Al_2O_3, 2.77–3.61 wt.% K_2O, and 7.40–8.31 wt.% $Na_2O + K_2O$. Compared with the hornblende–quartz monzonites, the porphyritic biotite granite samples have higher concentrations of SiO_2 (67.97–68.98 wt.%) and K_2O (3.92–4.17 wt.%), and lower Al_2O_3 (15.15–15.54 wt.%). In a total alkalis vs. SiO_2 (TAS) diagram

Table 3
Whole-rock geochemical data of intrusions from the Baoshan Cu-polymetallic deposit (major element: wt.%; trace elements: ppm).

Sample No.	BS23-1	BS23-2	BS15-1	BS15-2	BS23-3	BS23-4	BS15-3	BS15-4	BS23-5	BS23-6
Rock type	Hornblende quartz monzonite				Porphyritic biotite granite					
SiO_2	61.55	60.90	63.03	62.67	68.84	68.22	67.97	68.98	68.47	68.46
Al_2O_3	16.98	16.92	16.06	16.38	15.35	15.15	15.54	15.38	15.16	15.39
FeO	2.67	2.81	2.41	2.16	1.10	1.38	1.42	1.21	1.35	1.38
Fe_2O_3	1.38	1.50	1.69	1.55	1.16	1.05	1.09	0.98	1.30	1.15
MgO	2.60	2.80	2.52	2.28	0.91	1.04	1.08	0.94	1.19	1.11
CaO	4.72	4.82	4.11	4.02	2.38	2.52	2.60	2.42	2.67	2.60
Na_2O	4.63	4.55	4.61	4.71	4.48	4.54	4.39	4.42	4.39	4.46
K_2O	2.77	2.91	3.22	3.61	3.95	4.09	4.15	4.17	3.92	4.01
MnO	0.06	0.06	0.07	0.06	0.03	0.03	0.04	0.03	0.04	0.04
TiO_2	0.92	1.00	0.86	0.77	0.45	0.47	0.49	0.43	0.52	0.51
P_2O_5	0.06	0.06	0.07	0.06	0.03	0.03	0.04	0.03	0.04	0.04
LOI	1.27	1.25	1.01	1.37	1.06	1.18	0.91	0.72	0.66	0.58
Total	99.77	99.76	99.78	99.77	99.82	99.81	99.80	99.79	99.81	99.82
$Na_2O + K_2O$	7.40	7.46	7.83	8.31	8.43	8.63	8.54	8.58	8.31	8.47
A/NCK	0.88	0.87	0.87	0.86	0.96	0.92	0.95	0.95	0.93	0.94
A/NK	1.60	1.59	1.45	1.41	1.32	1.27	1.33	1.31	1.32	1.32
$Mg^{\#}$	54	55	53	53	43	44	44	45	46	45
Li	16.53	19.42	16.27	12.95	17.17	13.10	12.86	8.13	16.64	13.14
Be	1.79	1.79	2.64	2.13	3.57	3.06	3.65	2.73	3.24	2.32
Sc	7.93	8.58	6.50	5.96	3.66	3.70	4.68	2.97	4.64	2.80
V	73.39	81.43	87.82	80.71	43.51	37.88	51.93	47.62	53.84	48.89
Cr	37.75	40.01	44.19	32.60	15.80	13.23	17.88	12.40	19.74	10.96
Co	11.77	13.40	13.12	10.76	5.26	5.20	6.35	4.63	6.04	5.03
Ni	17.81	19.73	20.41	16.58	6.85	5.99	7.54	5.04	7.05	5.99
Cu	16.01	14.90	12.91	26.39	13.15	12.33	30.10	8.86	9.10	7.79
Zn	62.62	68.96	94.96	76.31	51.96	56.32	67.13	52.14	65.71	56.74
Ga	20.43	21.64	22.86	20.63	23.44	21.61	26.29	20.84	23.23	20.40
Rb	71.29	81.31	65.02	82.62	144.54	123.17	157.37	114.33	124.12	74.21
Sr	748.44	761.04	810.80	763.80	622.20	571.90	757.90	569.40	633.70	561.50
Y	8.78	10.47	10.37	11.12	16.76	14.87	24.44	12.57	15.94	15.70
Zr	164.65	216.02	209.65	209.72	172.13	199.17	185.74	176.49	186.26	179.43
Nb	7.04	7.94	9.37	8.08	11.60	10.32	15.30	9.92	11.29	9.63
Cs	1.90	2.61	2.48	2.39	3.19	2.54	2.69	1.77	2.10	1.74
Ba	754.60	801.60	900.60	914.76	838.00	796.39	988.48	790.97	817.00	723.43
La	26.31	31.52	28.59	32.18	32.55	26.84	32.97	29.30	32.66	30.93
Ce	52.06	61.74	55.69	61.78	57.33	50.86	65.21	52.82	61.54	59.55
Pr	5.88	7.10	6.77	7.27	6.37	6.00	7.66	6.00	7.10	6.97
Nd	22.22	26.44	25.55	27.33	23.03	21.07	27.49	21.09	25.65	25.08
Sm	3.81	4.65	4.17	4.58	3.89	3.56	4.98	3.39	4.24	4.23
Eu	0.92	1.14	1.04	1.08	0.87	0.82	1.04	0.75	0.98	0.95
Gd	2.95	3.56	3.33	3.78	3.56	3.36	4.52	3.26	3.77	3.40
Tb	0.40	0.48	0.45	0.47	0.56	0.50	0.77	0.46	0.57	0.51
Dy	1.80	2.10	2.10	2.48	2.87	2.54	4.20	2.20	2.86	2.76
Ho	0.30	0.37	0.39	0.43	0.58	0.51	0.85	0.44	0.56	0.54
Er	0.86	0.99	1.11	1.21	1.68	1.50	2.50	1.31	1.69	1.63
Tm	0.12	0.15	0.17	0.17	0.27	0.24	0.41	0.21	0.27	0.25
Yb	0.84	0.97	1.00	1.15	1.80	1.64	2.65	1.42	1.84	1.75
Lu	0.13	0.15	0.15	0.17	0.26	0.24	0.38	0.21	0.27	0.25
Hf	9.17	11.73	12.37	11.47	7.52	8.08	7.39	8.14	7.56	7.43
Ta	0.29	0.31	0.67	0.60	1.15	1.06	1.49	1.04	1.16	1.21
Pb	11.61	11.72	15.78	17.07	21.55	17.81	19.30	19.87	20.13	19.30
Bi	0.06	0.05	0.09	0.14	0.10	0.09	0.08	0.08	0.09	0.09
Th	13.54	13.22	10.90	10.46	25.01	20.75	24.94	20.12	23.33	17.43
U	3.52	3.94	3.88	3.60	10.36	8.20	14.29	6.76	9.36	6.56
∑REE	118.59	141.36	130.50	144.07	135.62	119.67	155.63	122.84	144.00	138.79
HREE	7.40	8.76	8.69	9.85	11.57	10.54	16.28	9.49	11.82	11.08
LREE	111.20	132.59	121.81	134.22	124.05	109.14	139.34	113.35	132.17	127.71
LREE/HREE	15.03	15.13	14.01	13.62	10.72	10.36	8.56	11.94	11.18	11.52
$(La/Yb)_N$	22.48	23.22	20.53	20.14	12.94	11.73	8.93	14.82	12.71	12.68
Sr/Y	85.23	72.69	78.19	68.68	37.12	38.46	31.01	45.30	39.76	35.76
δEu	0.81	0.83	0.83	0.77	0.71	0.72	0.66	0.68	0.74	0.74

Note: LOI: Loss on ignition; A/CNK = molecular $[Al_2O_3/(CaO + Na_2O + K_2O)]$; A/NK = molecular $[Al_2O_3/(Na_2O + K_2O)]$; $\delta Eu = Eu_N/(Gd_N + Sm_N)^{1/2}$; $(La/Yb)_N = (La/0.237)/(Yb/0.17)$; $Mg^{\#} = 100 \times$ molecular $Mg^{2+}/(Mg^{2+} + Fe^{2+})$.

(Fig. 8A; Middlemost, 1994), data for two types of samples plot at the junction of the quartz monzonite field with monzonite and granite fields, and are classified as subalkaline (Irvine and Baragar, 1971). The hornblende–quartz monzonite and porphyritic biotite granite samples are classified as potassic suites using a K_2O vs. Na_2O diagram(Fig. 8B; Middlemost, 1972). On a K_2O vs. SiO_2 variation diagram (Fig. 8C; Peccerillo and Taylor, 1976), data for all samples fall in the high-K calc-alkaline series. Their A/CNK values range from 0.86–0.96, and plot within the metaluminous field in an A/NK vs. A/CNK diagram (Fig. 8D; Maniar and Piccoli, 1989).

The rocks analyzed here have relatively low total rare earth element (REE) abundances (ΣREE = 118.59–155.63 ppm; Table 3), and display coherent chondrite-normalized rare earth element (REE) patterns. These patterns are characterized by light rare earth ele-

Table 4
Hf isotopic data for zircons from intrusions from the Baoshan Cu-polymetallic deposit.

Spot	Age/Ma	$^{176}Yb/^{177}Hf$	2σ	$^{176}Lu/^{177}Hf$	2σ	$^{176}Hf/^{177}Hf$	2σ	$^{176}Hf/^{177}Hfi$	eHf(0)	eHf(t)	T_{DM} (Ma)	T^{C}_{DM}(Ma)	$f_{Lu/Hf}$
BZ23-1, hornblende–quartz monzonite, 252.45 ± 0.70 Ma													
BZ23-1-01	252.7	0.016854	0.000111	0.000645	0.000005	0.282687	0.000026	0.282684	−3.0	2.4	794	1122	−0.98
BZ23-1-02	250.3	0.013574	0.000063	0.000515	0.000003	0.282667	0.000027	0.282664	−3.7	1.7	819	1168	−0.98
BZ23-1-03	251.0	0.017495	0.000430	0.000658	0.000017	0.282705	0.000030	0.282702	−2.4	3.0	769	1082	−0.98
BZ23-1-04	252.8	0.010705	0.000145	0.000410	0.000005	0.282660	0.000029	0.282658	−4.0	1.5	826	1179	−0.99
BZ23-1-05	253.7	0.015711	0.000069	0.000593	0.000003	0.282687	0.000031	0.282684	−3.0	2.5	793	1121	−0.98
BZ23-1-06	252.1	0.008158	0.000072	0.000320	0.000003	0.282667	0.000026	0.282666	−3.7	1.8	814	1163	−0.99
BZ23-1-07	253.8	0.014054	0.000093	0.000529	0.000004	0.282648	0.000026	0.282645	−4.4	1.1	846	1208	−0.98
BZ23-1-08	252.6	0.015594	0.000253	0.000581	0.000009	0.282640	0.000030	0.282637	−4.7	0.8	858	1227	−0.98
BZ23-1-09	252.2	0.010740	0.000519	0.000414	0.000020	0.282664	0.000025	0.282662	−3.8	1.6	821	1171	−0.99
BZ23-1-10	252.3	0.015623	0.000030	0.000580	0.000001	0.282674	0.000027	0.282671	−3.5	2.0	811	1151	−0.98
BZ23-1-11	251.7	0.015195	0.000053	0.000562	0.000002	0.282657	0.000026	0.282655	−4.1	1.4	833	1188	−0.98
BZ23-1-12	252.8	0.009027	0.000093	0.000338	0.000003	0.282659	0.000028	0.282657	−4.0	1.5	826	1181	−0.99
BZ23-1-13	251.7	0.008614	0.000044	0.000331	0.000002	0.282633	0.000025	0.282632	−4.9	0.6	862	1240	−0.99
BZ23-1-14	253.3	0.014296	0.000082	0.000518	0.000004	0.282690	0.000028	0.282688	−2.9	2.6	786	1112	−0.98
BZ23-1-15	251.6	0.013779	0.000020	0.000501	0.000000	0.282686	0.000025	0.282683	−3.1	2.4	793	1124	−0.98
BZ23-1-16	252.2	0.012039	0.000272	0.000444	0.000009	0.282656	0.000025	0.282654	−4.1	1.4	833	1190	−0.99
BZ23-1-17	252.9	0.016585	0.000193	0.000622	0.000007	0.282703	0.000024	0.282700	−2.5	3.0	771	1086	−0.98
BZ23-1-18	253.3	0.033235	0.001576	0.001227	0.000058	0.282692	0.000030	0.282686	−2.8	2.5	799	1117	−0.96
BZ23-1-19	252.2	0.008819	0.000373	0.000342	0.000013	0.282662	0.000025	0.282660	−3.9	1.6	822	1176	−0.99
BZ23-1-20	252.6	0.007498	0.000042	0.000295	0.000002	0.282621	0.000029	0.282620	−5.3	0.2	877	1265	−0.99
BZ23-1-21	252.0	0.005454	0.000012	0.000221	0.000000	0.282631	0.000024	0.282630	−5.0	0.5	862	1243	−0.99
BZ23-1-22	252.0	0.008901	0.000067	0.000350	0.000003	0.282672	0.000028	0.282670	−3.5	1.9	809	1154	−0.99
BZ23-1-23	252.7	0.023182	0.000294	0.000884	0.000011	0.282656	0.000027	0.282651	−4.1	1.3	843	1195	−0.97
BZ23-2, porphyritic biotite granite, 251.10 ± 0.98 Ma													
BZ23-2-01	251.4	0.005166	0.000034	0.000213	0.000001	0.282630	0.000014	0.282629	−5.0	0.5	863	1245	−0.99
BZ23-2-02	251.9	0.018424	0.001015	0.000792	0.000050	0.282535	0.000029	0.282532	−8.4	−3.0	1009	1464	−0.98
BZ23-2-03	251.2	0.012757	0.000238	0.000506	0.000011	0.282611	0.000017	0.282609	−5.7	−0.3	896	1291	−0.98
BZ23-2-04	251.7	0.009506	0.000191	0.000368	0.000007	0.282586	0.000020	0.282584	−6.6	−1.1	928	1346	−0.99
BZ23-2-05	251.3	0.006155	0.000062	0.000238	0.000002	0.282560	0.000022	0.282559	−7.5	−2.0	961	1403	−0.99
BZ23-2-06	248.0	0.029629	0.001580	0.001271	0.000082	0.282498	0.000039	0.282492	−9.7	−4.5	1075	1555	−0.96
BZ23-2-07	251.2	0.013338	0.000273	0.000514	0.000009	0.282507	0.000037	0.282505	−9.4	−3.9	1041	1524	−0.98
BZ23-2-08	251.2	0.023520	0.000431	0.000917	0.000015	0.282556	0.000017	0.282552	−7.6	−2.3	984	1419	−0.97
BZ23-2-09	251.1	0.034625	0.003324	0.001301	0.000110	0.282469	0.000018	0.282463	−10.7	−5.4	1117	1618	−0.96
BZ23-2-10	250.8	0.010526	0.000085	0.000400	0.000003	0.282605	0.000018	0.282603	−5.9	−0.5	902	1304	−0.99
BZ23-2-11	249.2	0.013603	0.000238	0.000509	0.000009	0.282650	0.000016	0.282647	−4.3	1.1	843	1206	−0.98
BZ23-2-12	252.0	0.021641	0.000637	0.000966	0.000025	0.282491	0.000018	0.282486	−10.0	−4.6	1077	1566	−0.97
BZ23-2-13	251.3	0.008108	0.000117	0.000305	0.000005	0.282649	0.000016	0.282647	−4.4	1.1	840	1205	−0.99
BZ23-2-14	251.1	0.011899	0.000344	0.000476	0.000015	0.282606	0.000014	0.282604	−5.9	−0.4	902	1302	−0.99
BZ23-2-15	251.5	0.013583	0.000418	0.000495	0.000015	0.282581	0.000019	0.282578	−6.8	−1.3	939	1360	−0.99

$\varepsilon_{Hf}(t)=10000\times(([^{176}Hf/^{177}Hf)_S-(^{176}Lu/^{177}Hf)_S\times(e^{\lambda t}-1)]/[(^{176}Hf/^{177}Hf)_{CHUR,0}-(^{176}Lu/^{177}Hf)_{CHUR}\times((e^{\lambda t}-1)]-1\}$, $T_{DM}=1/\lambda\times In\{1+[(^{176}Hf/^{177}Hf)_S-(^{176}Hf/^{177}Hf)_{DM}]/[(^{176}Hf/^{177}Hf)_S-(^{176}Hf/^{177}Hf)_{DM}]$, $T^{C}_{DM}=T_{DM}-(T_{DM}-t)\times[(f_{cc}-f_s)/(f_{cc}-f_{DM})$, $f_{Lu/Hf}=(^{176}Lu/^{177}Hf)_S/(^{176}Lu/^{177}Hf)_{CHUR}-1$, where, $\lambda=1.867\times10^{-11}/year^{-1}$ (Soderlund et al., 2004); $(^{176}Lu/^{177}Hf)_S$ and $(^{176}Hf/^{177}Hf)_S$ are the measured values of the samples; $(^{176}Lu/^{177}Hf)_{CHUR}=0.0332$ and $(^{176}Hf/^{177}Hf)_{CHUR,\ 0}=0.282772$ (Blichert-Toft and Albarède, 1997); $(^{176}Lu/^{177}Hf)_{DM}=0.0384$ and $(^{176}Hf/^{177}Hf)_{DM}=0.28325$ (Griffin et al., 2002); $(^{176}Lu/^{177}Hf)_{mean\ crust}=0.015$; $f_{cc}=[(^{176}Lu/^{177}Hf)_{mean\ crust}/(^{176}Lu/^{177}Hf)_{CHUR}]-1$; $f_s=f_{Lu/Hf}$; $f_{DM}=[(^{176}Lu/^{177}Hf)_{DM}/(^{176}Lu/^{177}Hf)_{CHUR}]-1$; and t = crystallization time of zircon.

ment (LREE) enrichment and heavy rare earth element (HREE) depletion (Fig. 8E; Boynton, 1984). The porphyritic biotite granite samples are moderately fractionated, yielding LREE/HREE ratios of 8.56–11.94, and $(La/Yb)_N$ ratios of 8.93–14.82, and weakly negative Eu anomalies (δEu = 0.66–0.74), indicative of the fractional crystallization of plagioclase (Lightfoot et al., 1987; Li, 1992). In comparison, the hornblende–quartz monzonite samples have higher degrees of fractionation between LREEs and HREEs, with smaller negative Eu anomalies (δEu = 0.77–0.83), LREE/HREE ratios of 13.62–15.13, $(La/Yb)_N$ ratios of 20.14–23.22, and relatively low concentrations of Y and Yb, suggesting the presence of residual garnet in the magma source (Otamendi et al., 2002; Xiong et al., 2005a,b).

In a primitive mantle–normalized trace element spider diagram (Fig. 8F; Sun and McDonough, 1989), the hornblende–quartz monzonite samples are enriched in Th, U, and large ion lithophile elements (LILEs; e.g., Rb and K) and depleted in high field strength elements (HFSEs; e.g., Nb, Ta, P, and Ti). However, the trace element composition of porphyritic biotite granite samples reveal higher concentrations of Rb, Th, U, and Ta, but lower concentrations of Ba than the host hornblende–quartz monzonite. The variation in concentrations of Ta across the hornblende–quartz monzonite samples suggests that fractional crystallization of Ti-bearing minerals occurred, leading to Ta enrichment during magmatic evolution (Li, 1992; Zhao, 1997). Middle Permian–Middle Triassic granites in the Yichun–Hegang region(Wei, 2012), south of the study area, are high-K calc-alkaline and sub-alkaline rocks, and have similar concentrations of trace elements and REE as the igneous rocks of the Baoshan Cu–polymetallic deposit (Shaded area in Fig. 8).

5.4. Zircon Lu–Hf isotopic data

Lu–Hf isotopic analyses of zircons from the hornblende–quartz monzonite (BZ23-1) and porphyritic biotite granite (BZ23-2) samples are shown in Fig. 9, and the zircon Hf isotopic data and calculation results are presented in Table 4. The magmatic zircons from hornblende–quartz monzonite (252.45 ± 0.70 Ma) show a narrow range of Hf isotopic compositions, with $^{176}Hf/^{177}Hf$ ratios ranging from 0.282620 to 0.282702. The $\varepsilon_{Hf}(t)$ values and T^{C}_{DM} ages ranged from +0.1 to +3.1 and from 1081 to 1267 Ma, respectively (Fig. 9). The magmatic zircons from porphyritic biotite granite (251.10 ± 0.98 Ma) have $^{176}Hf/^{177}Hf$ ratios that vary from 0.282469 to 0.282650, and $\varepsilon_{Hf}(t)$ values from −5.4 to +1.1. T^{C}_{DM} ages of the por-

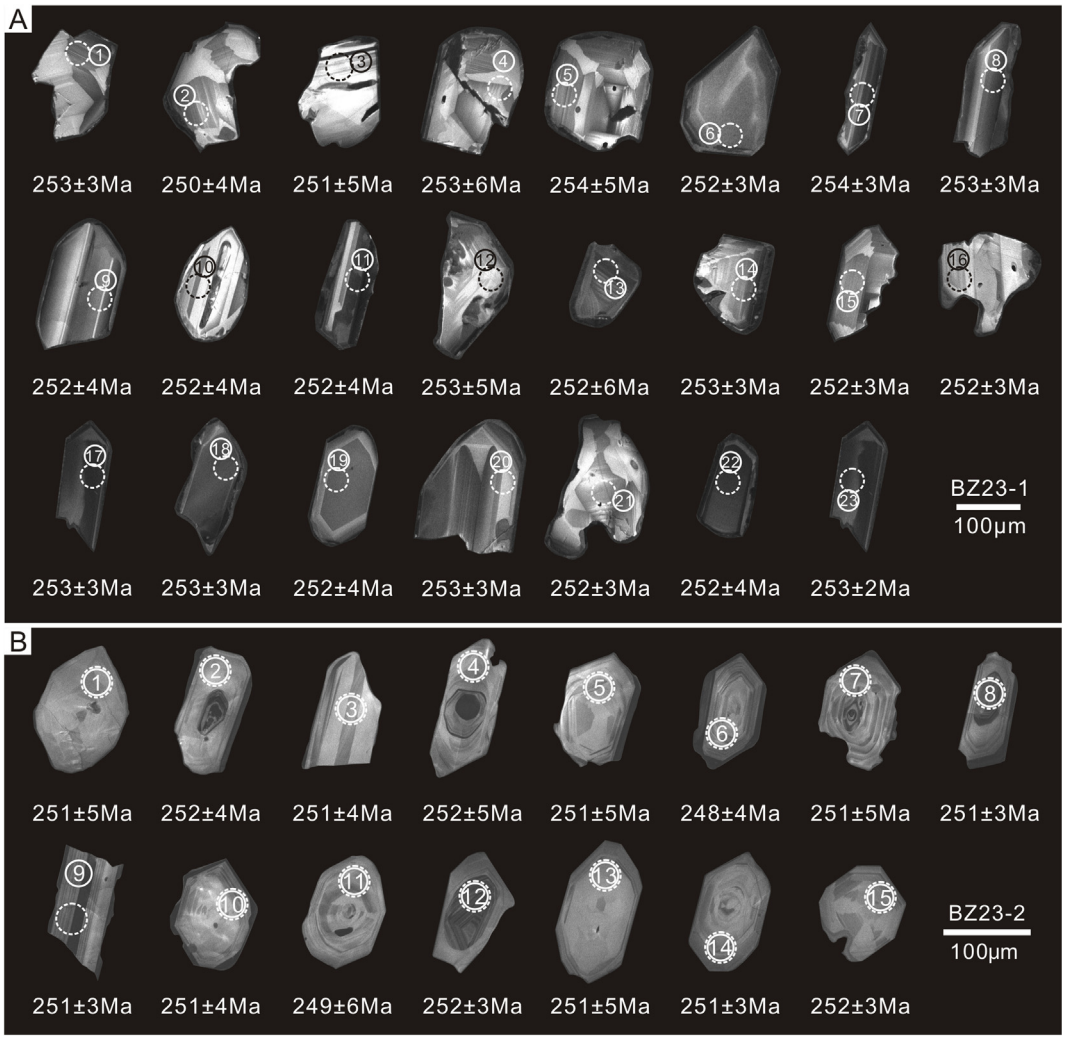

Fig. 5. Cathodoluminescence (CL) images of zircons from (A) hornblende–quartz monzonite and (B) porphyritic biotite granite of the Baoshan Cu–polymetallic deposit. The full line represent U–Pb age analytical spot, dash line represent Hf isotope analytical spot.

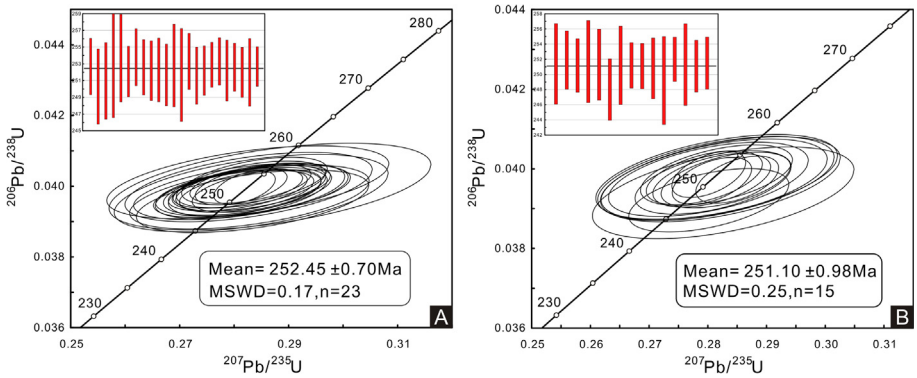

Fig. 6. Concordia diagrams of zircon U–Pb ages for (A) hornblende–quartz monzonite and (B) porphyritic biotite granite of the Baoshan Cu–polymetallic deposit.

phyritic biotite granite range from 1205 to 1618 Ma (Fig. 9), which is older than the hornblende–quartz monzonite. The analyzed zircons have similar Hf isotopic compositions to zircons from Phanerozoic igneous rocks in the CAOB (Fig. 9A; Xiao et al., 2004; Chen et al., 2009; Yu et al., 2012), but are different to those of the Neoarchean and Paleoproterozoic in the Paleozoic–Late Mesozoic strata of the Yanshan fold and thrust belt (Yang et al., 2006).

6. Discussion

6.1. Timing, geodynamic setting of magmatism and mineralization

The timing of magmatism and mineralization is important when considering ore deposit genesis, metallogenetic geodynamical setting, regional metallogenic regularity, and in guiding mining

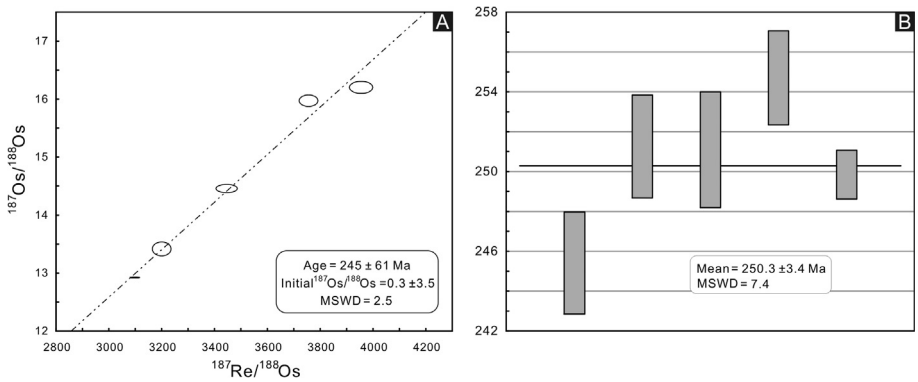

Fig. 7. (A) Re–Os isochron and (B) weighted mean model ages of molybdenite from the Baoshan Cu–polymetallic deposit.

exploration. In this study, the zircons from the Baoshan intrusions are euhedral–subhedral, and exhibit oscillatory growth zoning (Fig. 5) and high Th/U ratios. These features suggest that the zircon U–Pb ages represent the crystallization age of these intrusions. Our new age data for the hornblende–quartz monzonite and porphyritic biotite granite are 252.45 ± 0.70 Ma and 251.10 ± 0.98 Ma, respectively. Five molybdenite samples yield a weighted age of 250.3 ± 3.4 Ma. The zircon U–Pb and molybdenite Re–Os ages are concordant within error, indicating that magmatism and mineralization of the Baoshan Cu–polymetallic deposit occurred during the Late Permian–Early Triassic. Numerous geochronological data have been obtained for hydrothermal deposits in the Lesser Xing'an Range, and it is widely reported that porphyry and skarn deposits were formed in the Early–Middle Jurassic, while epithermal deposit formation was concentrated in the Early Cretaceous (Zhang et al., 2010; Shao et al., 2011; Ma and Chen, 2012; Chen et al., 2012; Yang et al., 2012; Sun et al., 2013a,b; Hu et al., 2014a,b; Sun et al., 2014; Hao et al., 2016). Data relating to Late Permian–Early Triassic mineralization are generally lacking. During extensive exploration in recent years, the Baoshan skarn Cu–polymetallic deposit and Gaoganshan porphyry Mo deposit (Re–Os: 250.2 ± 1.4 Ma, Zhang et al., 2017; 250.7 ± 1.8 Ma, Hao et al., 2015) have been discovered in the northern Lesser Xing'an Range. These new discoveries not only provide data relating to Late Permian–Early Triassic mineralization in the Lesser Xing'an Range, but also indicate a need for further exploration.

The study area is located in the eastern segment of the CAOB, which is situated between the North China Craton and Siberian Craton. The tectonic history of the region is dominated by the evolution of the Paleo-Asian Ocean during the Paleozoic, closure of the Mongol–Okhotsk Ocean in the Late Paleozoic–Mesozoic, and superposition of Mesozoic subduction of the Pacific Plate in the Mesozoic–Cenozoic (Wu et al., 1999, 2011; Li, 2006; Xu et al., 2012; Sun et al., 2013a,b). The tectonic framework of the study area was mainly controlled by the evolution of the Paleo-Asian Ocean, which was characterized by a large-scale island arc system and continental margin accretion (Ren et al., 1999; Liu et al., 2004). However, the timing and position of the closure of the Paleo-Asian Ocean have long been controversial. In recent decades, many studies have investigated the tectonic setting and evolution, sedimentology, magmatism, structural deformation, paleobiogeography, and paleomagnetism of the CAOB. Data support the interpretation that complete closure of the Paleo-Asian Ocean took place from the Late Permian–Early Triassic, and the Suolunshan–Xar Moron River–Changchun–Yanji Belt represents the final suture zone between the North China Craton and Siberia Craton (Wu et al., 2007b; Sun et al., 2004b; Xiao et al., 2003, 2009; Li, 2006; Zhang et al., 2009a,b; Liu et al., 2010; Chen et al., 2013; Cao et al., 2013). Since the Jurassic, NE China has been tectonically overprinted by westward subduction of the Pacific Plate (Zhao et al., 1994; Isozaki, 1997; Zhou et al., 2009; Wu et al., 2011; Xu et al., 2012).

The regional stratigraphy of the northern Lesser Xing'an Range is characterized by a Permian terrigenous clastic–carbonate formation and Cretaceous continental intermediate–felsic volcanic rocks (HBGMR, 1993; Han et al., 1995). The absence of Triassic and Jurassic strata indicates that the study area was undergoing continental collisional orogenesis during this period. According to the study of the geochronology and geochemisytry of granitic rocks in the Yichun-Hegang area, Wei (2012) pointed out that the Middle Permian to Middle Triassic granitoids were related to collision of North China Craton and Siberian Craton. In addiation, Zhang et al. (2017) considered that the newly discovered Gaogangshan Mo deposit is a Permian-Triassic collision-type porphyry Mo deposit in the Lesser Xing'an Range metallogenic belt. This study considers new geochronological data, together with existing knowledge of the regional tectonics, and we suggest that the formation of the Baoshan Cu–polymetallic deposit was related to the Late Permian–Early Triassic continental collision between the North China Craton and Songnen Block, during or after the closure of the Paleo-Asian Ocean. Both the hornblende–quartz monzonite and porphyritic biotite granite samples plot within the volcanic arc granite field on a Rb vs. (Yb + Ta) diagram (Fig. 11E; Pearce et al., 1984), and on a Rb vs. (Y + Nb) diagram within the post-collision granite field (Fig. 11F), indicating that the Baoshan intrusions were likely generated in the same tectonic setting. Therefore, we infer that the diagenesis and mineralization of the Baoshan Cu–polymetallic deposit took place in a transitional tectonic setting from collisional orogeny to extension, and after collision between the North China Craton and the Songnen Block, during the latter stages of the Xingmeng orogeny.

6.2. Petrogenesis and source of the magma

Ascertaining the genetic type of granitoids is significant to understanding the magma source region, magmatic process, and tectonic setting (Pearce et al., 1984; Sylvester, 1998; Barbarin, 1999). All of the Baoshan intrusion samples are metaluminous, with a narrow range of A/CNK ratios (A/CNK = 0.86–0.96; Fig. 8D), and are classified as I-type granites (Chappell and White, 2001). In addition, P_2O_5 concentration of the Baoshan samples decrease with increasing SiO_2 concentration (Fig. 10A). The concentration of Th increases with increasing Rb (Fig. 10B), and these patterns are consistent with the evolution of I-type magmas (Chappell and White, 1992; Li et al., 2007). Moreover, in a Ce + Y + Nb + Zr vs. TFeO/MgO and ($K_2O + Na_2O$)/CaO petrogenetic discrimination diagrams (Fig. 10C, D), the Baoshan intrusion samples plot in the field of I-type granites, rather than that of A-type granites. Therefore, we

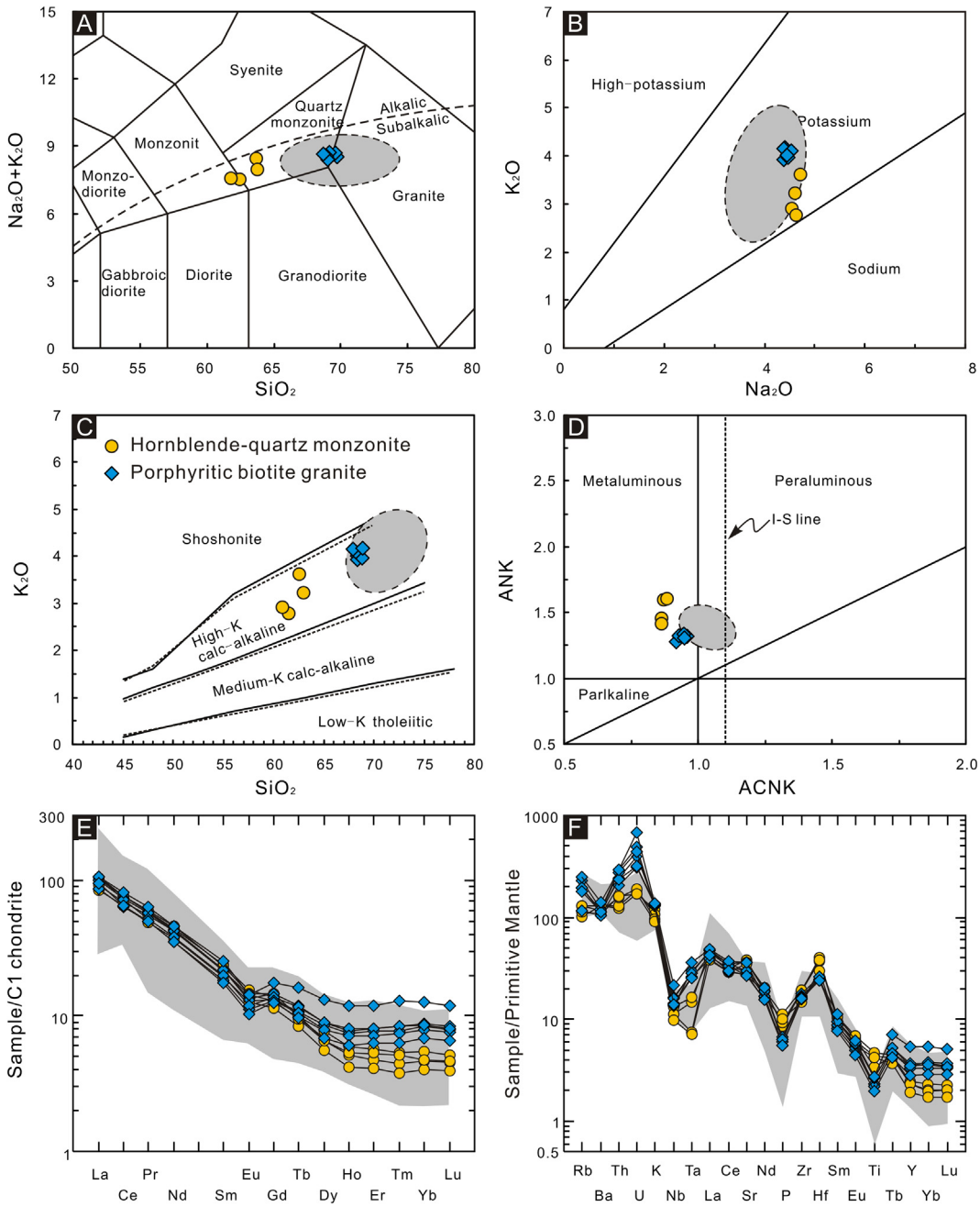

Fig. 8. (A) SiO_2 versus ($Na_2O + K_2O$) plot (Middlemost 1994). (B) Na_2O versus K_2O plot (Middlemost, 1972). (C) SiO_2 versus K_2O plot (Peccerillo and Taylor, 1976). (D) A/CNK versus A/NK plot (Maniar and Piccoli, 1989). (E) Chondrite–normalized REE patterns (normalized values are from Boynton, 1984). (F) Primitive–mantle–normalized trace element patterns (normalized values are from Sun and McDonough, 1989). The shaded areas assoceiated with granite in Yichun–Hegang area is quoted from Wei, 2012.

conclude that the Baoshan intrusions are metaluminous, high-K calc-alkaline I-type granites. This interpretation is supported by the presence of amphibole and biotite, and the absence of cordierite and muscovite.

Experimental petrology has shown that high-K calc-alkaline I-type granitoids are typically formed by the partial melting of hydrous calc-alkaline to high-K calc-alkaline, basaltic to intermediate metamorphic rocks within the crust (Patiño Douce and Harris, 1998; Patiño Douce and McCarty, 1998). No mafic rocks are found in association with the granitic intrusions in the mining area or outside it, precluding the possibility that granitic intrusions were generated solely by the fractional crystallization of mafic magmas. Additionally, in a Th/Nd vs. Th plot (Fig. 11A), the Baoshan intrusion samples show a sloping trend, suggesting partial melting or magma mixing was the dominant process during magmatic evolution.

The geochemical characteristics of the hornblende–quartz monzonite and porphyritic biotite granites also show obvious differences. In Sr/Y vs. Y and $(La/Yb)_N$ vs. Yb_N petrogenetic discrimination diagrams (Fig. 11C, D), the hornblende–quartz monzonite samples plot in the adakitic field, whereas the porphyritic biotite granite samples plot in the island arc calc-alkaline field. This suggests that the former have a different source and/or history than the latter. This interpretation is further supported by a $(La/Yb)_N$ vs. $(Yb)_N$ diagram, where hornblende–quartz monzonite samples plot in the field defined by magmas associated

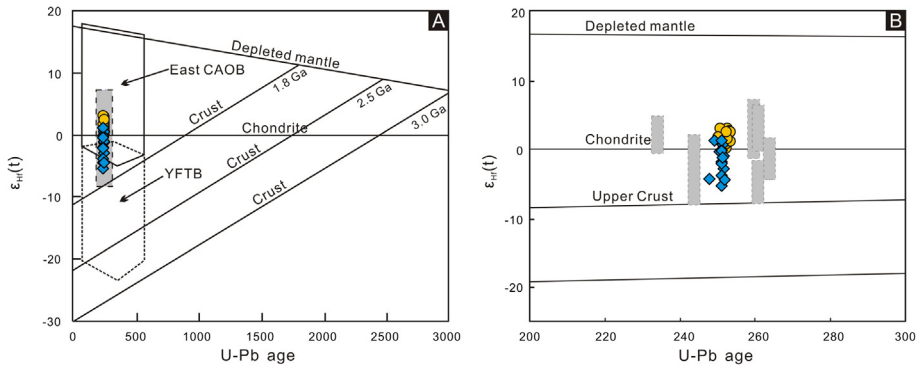

Fig. 9. $\varepsilon_{Hf}(t)$ versus crystallization age of zircons (A, B) for the Baoshan Cu–polymetallic deposit. The shaded areas assoceiated with granite in Yichun–Hegang area is quoted from Wei, 2012.

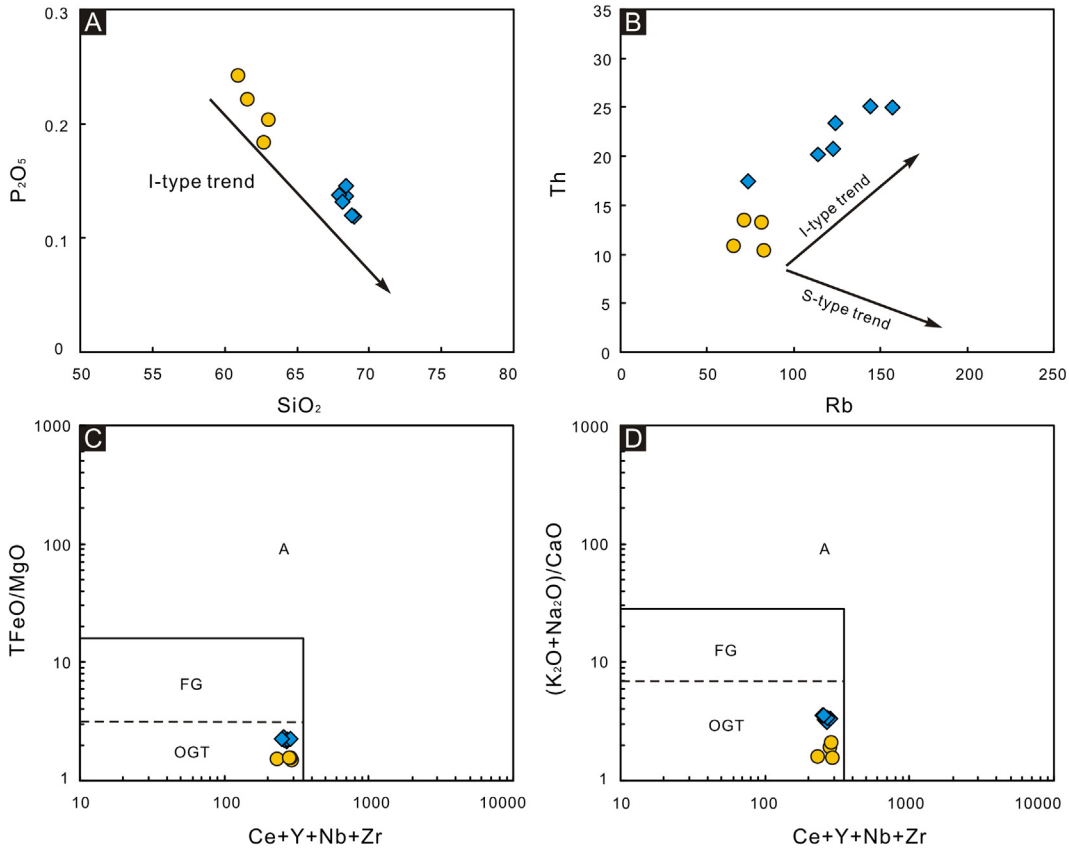

Fig. 10. (A) SiO_2 versus P_2O_5 plot. (B) Rb versus Th plot (Li et al., 2007). (C) TFeO/MgO versus Ce + Y + Nb + Zr plot (Whalen et al., 1987). (D) (K_2O + Na_2O)/CaO versus Ce + Y + Nb + Zr plot (Whalen et al., 1987).

with garnet–amphibole to amphibole residual phases, but porphyritic biotite granite samples are associated with amphibole-only residual phases. The highly fractionated REE patterns (LREE/HREE = 13.62–15.13; $(La/Yb)_N$ = 20.14–23.22), depletion in Y (8.78–11.12 ppm) and Yb (0.84–1.15 ppm), enrichment in Sr (748.44–761.04 ppm), and high Sr/Y ratios (68.68–85.23) of the hornblende–quartz monzonites also indicate that they are geochemically similar to adakites (Defant and Drummond, 1990). Although adakites are generally believed to form by partial melting of a subducted young and hot oceanic slab (Defant and Drummond, 1990; Sajona and Maury, 1998), other models for the genesis of adakites have been suggested, including from thickened lower crust (Zhang et al., 2001; Xiong et al., 2001, 2005a,b; Zhao et al., 2006), or delaminated lower continental crust (Kay and Kay, 1993; Xu et al., 2002; Gao et al., 2004; Wu et al., 2004). The hornblende–quartz monzonites have high concentrations K_2O (2.77–3.61 wt.%) and low Na_2O/K_2O ratios (1.31–1.67), which are inconsistent with slab-derived adakitic magmas (Na_2O/K_2O > 2; Zhang et al., 2001; Wang et al., 2001). In a SiO_2 vs. MgO diagram, the hornblende–quartz monzonite samples fall within the range of adakitic rocks formed by partial melting of delaminated lower crust (Fig. 11B; Rapp and Watson, 1995; Rapp et al., 1999; Martin et al., 2005; Wang et al., 2006). In addition, the relatively high MgO (2.52–2.80 wt.%), $Mg^{\#}$ (53.41–54.53), V (73.39–87.82 ppm), Cr (32.60–44.19 ppm), Co (10.76–13.40 ppm), and Ni (16.58–20.41 ppm) contents in the hornblende–quartz monzonites are similar to adakites derived from the partial melting of delaminated lower crust. In this case, a delaminated section of

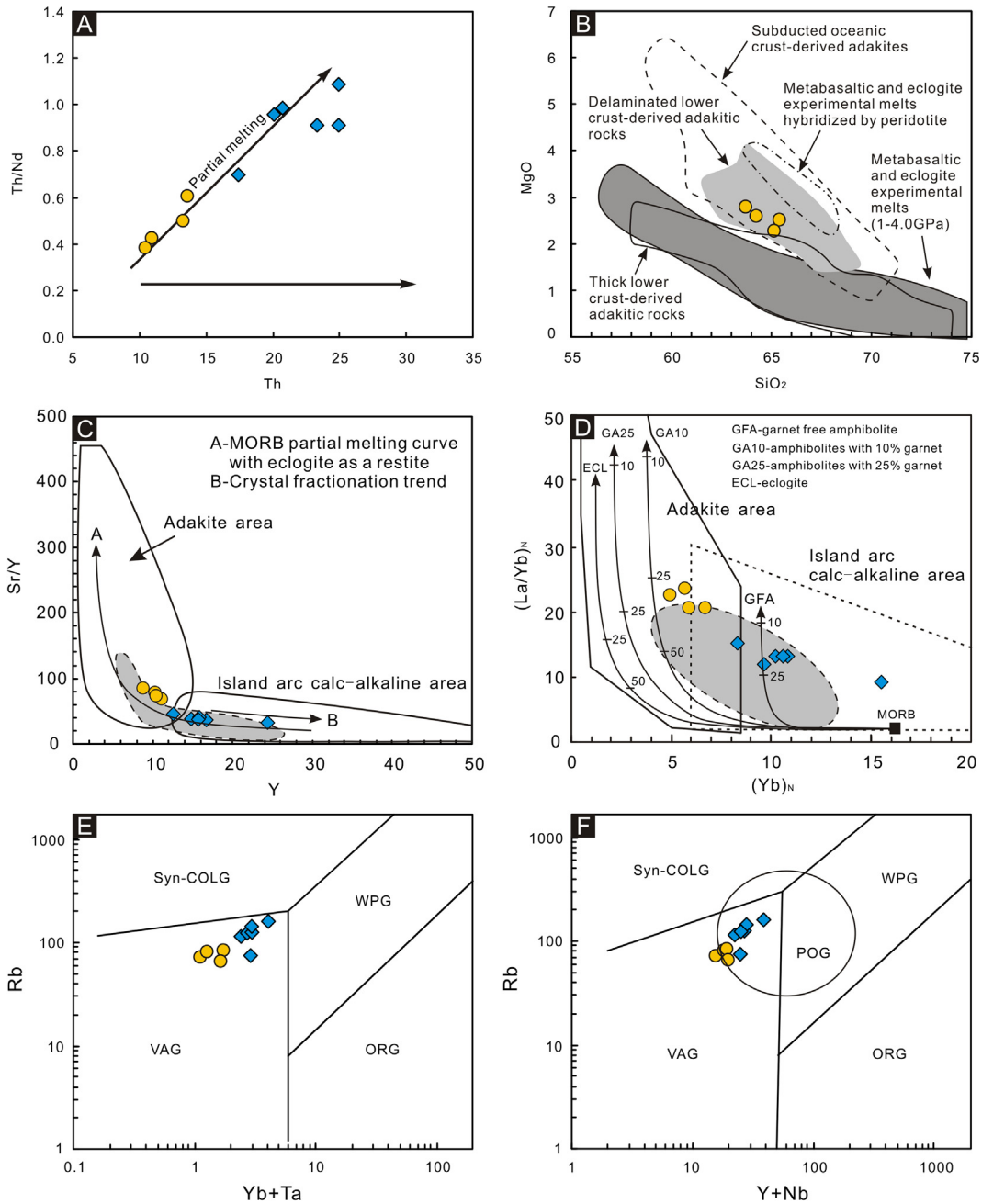

Fig. 11. (A) Th versus Th/Nd plot (Schiano et al., 2010). (B) SiO_2 versus MgO plot (Rapp and Watson, 1995; Rapp et al., 1999; Martin et al., 2005; Wang et al., 2006). (C) Sr/Y versus Y plot (Defant and Drummond, 1990). (D) $(La/Yb)_N$ versus $(Y)_N$ plot (Defant and Drummond, 1990). (E) Yb + Ta versus Rb plot (Pearce et al., 1984). (E) Y + Nb versus Rb plot (Pearce et al., 1984). The shaded areas assoceiated with granite in Yichun–Hegang area is quoted from Wei, 2012.

the lower crust is heated by the relatively hot mantle and can be partially melted (Kay and Kay, 1993). The melt passes through the mantle as it rises to the surface, resulting in elevated MgO, Ni, and Cr contents via interaction with mantle peridotites (Kepezhinskas et al., 1995; Smithies, 2000; Defant and Kepezhinskas, 2001; Defant et al., 2002; Xu et al., 2002; Gao et al., 2004).

Previous studies have shown that Nb/Ta ratios can be very useful in determining source regions (Eby et al., 1998). Nb/Ta ratios of the hornblende–quartz monzonites (13.45–25.77) are close to the average of the mantle (17.5; Sun and McDonough, 1989), indicating that they are generally mantle–derived magmas, while the Nb/Ta ratios of the porphyritic biotite granites (7.95–10.25) are closer to the average of crust (11; Taylor and Mclennan, 1985), favoring a crustal origin. In addiation, $Mg^{\#}$ values are a useful criterion for distinguishing melt derived from crustal material alone or from crustal material contaminated by mantle material. Melts that form by the partial melting of basaltic lower crust usually have a lower $Mg^{\#}$ (<40) than those contaminated by mantle material ($Mg^{\#}$ > 40; Rapp and Watson, 1995; Rapp et al., 1999; Guan et al., 2011; Zhu et al., 2009). All the porphyritic biotite granite samples of the present study have high $Mg^{\#}$ values (43–46), indicating the involvement of mantle material. Based on the above, the porphyritic biotite granites have the geochemical characteristics of island arc calc-alkaline magmas, and they may be derived from magma mixing.

These results are also supported by the zircon Hf isotopic data, and the similarities with the Hf isotopic compositions of the

Middle Permian–Middle Triassic granites in the Lesser Xing'an Range (The shaded area in Fig. 9; Wei, 2012). The Hf isotopic compositions of the hornblende–quartz monzonites are characterized by positive $\varepsilon_{Hf}(t)$ values (+0.1 to +3.1) and relatively young Hf model ages (T^{C}_{DM} = 1081–1267 Ma), suggesting that the primary magmas originated from a depleted mantle or newly underplated basaltic crust. The porphyritic biotite granites possess heterogeneous $\varepsilon_{Hf}(t)$ values that range from −5.4 to +1.1, and corresponding T^{C}_{DM} ages are between 1205 and 1618 Ma. Most $\varepsilon_{Hf}(t)$ values of the porphyritic biotite granites are negative, indicating a contribution of ancient crustal materials to their petrogenesis. Moreover, the several positive $\varepsilon_{Hf}(t)$ values from the porphyritic biotite granites are consistent with the hornblende–quartz monzonites, and imply the input of mantle material.

Taking all the above evidence into account, we conclude that the Late Permian–Early Triassic continental–continental collision caused over thickening and delamination of the lower crust. Partial melting of delaminated lower crust formed the primary adakitic magmas, and the adakitic magma may have reacted with surrounding mantle peridotites during ascent. Hornblende–quartz monzonite was formed by the emplacement of the adakitic magmas, whereas the porphyritic biotite granite formed by the mixing of adakitic magmas with a large amount of ancient crustal material during ascent.

6.3. Magmatism constraints on ore formation

Previous studies have shown that hydrous, sulfur-rich adakitic magmas, with high oxygen fugacity, are closely associated with Cu–Au mineralization (Oyarzun et al., 2001; Mungall, 2002; Wang et al., 2007). Interactions between the adakitic magmas and mantle peridotites likely took place during ascent of the adakitic magmas through the mantle. We infer this from the elevated concentrations of MgO, Cr, and Ni in the adakitic magmas. In addition, the Fe_2O_3 content of the adakitic magmas was likely released into the mantle, and the oxygen fugacity of the latter increased. This increase in oxygen fugacity oxidized metallic sulfides in the mantle, and chalcophile elements such as Cu were incorporated into the adakitic magmas. A large number of ore-forming elements released from the magma during its ascent and evolution are favorable for extensive Cu–Au mineralization (Wyborn and Sun, 1994; Sun et al., 2004c). Therefore, the ascent of the adakitic magmas enriched in ore-forming elements (e.g., Cu), provided the mineralization material for the Baoshan Cu–polymetallic deposit. This explains why the dominant ore element of the Baoshan deposit is copper, and different from the other skarn-type deposits in the study area. In addition, Ni vs. V and Sc vs. Rb diagrams show that the hornblende–quartz monzonites are in accordance with those of typical skarn-type Cu deposits worldwide (Fig. 12; Meinert, 1995), also indicating that the Cu mineralization was likely related to the hornblende–quartz monzonites. Although the emplacement ages of the hornblende–quartz monzonite and the porphyritic biotite granite are concordant, the former is more widespread in the mining area, and the skarn-type orebodies are hosted in the contact zone between the hornblende–quartz monzonites and the dolomitic crystalline limestones. In summary, the adakitic hornblende–quartz monzonites provided ideal conditions for the formation of the Baoshan Cu–polymetallic deposit.

Considering the regional geological history, geological features of the deposit, and our new geochemical and geochronological data, we consider that the Baoshan Cu–polymetallic deposit was formed in a Late Permian–Early Triassic continental collisional regime, during or after the closure of the Paleo-Asian Ocean. The lower crust at this time was likely overthickened, as a consequence of continental collision between the North China Craton and Songnen Block. The increase in pressure and temperature under such conditions likely led to metamorphism of mafic rocks in the lower crust into amphibole-bearing eclogites. The high density of such amphibole-bearing mafic rocks in the lower crust then led to delamination (Kay and Kay, 1993; Xu et al., 2002; Wang et al., 2004, 2006). Adakitic magmas most likely originated from partial melting of delaminated lower crust, with garnet being the main residual mineral and little to no plagioclase (Bergantz, 1989). Interactions between adakitic magmas and mantle peridotites occurred during the ascent of adakitic magmas through the mantle, resulting in oxidation of metallic sulfides, and incorporation of chalcophile elements, such as Cu, into the magmas. With the emplacement of the adakitic magmas, hydrothermal fluids exsolved from the magma and caused extensive alteration, forming skarns and associated mineralization in the contact zone between the hornblende–quartz monzonite and dolomitic crystalline limestones. The difference in chemical activity of various elements means that a variety of orebodies can be formed in different structural zones during different stages of mineralization. In addition, mixed magma comprising both adakitic magmas and ancient crustal materials was emplaced into the shallow crust, and caused the formation of the porphyritic biotite granite (Fig. 13).

The wall rock in the Baoshan area is the Lower Cambrian Qianshan Formation, which consists predominantly of dolomitic crystalline limestones, sandstones, siltstones, and slates. The well-developed interbedded structure was favorable for the transportation of ore-forming fluids and metasomatism, and provided a suitable location for the precipitation of ore-forming materials. Large-scale alteration and mineralization occurred near the contact zone between the intrusions and limestones, and the widely distributed alteration minerals also provided conditions for the precipitation of the ore-forming materials. Furthermore, minor porphyry-type mineralization and related alteration have been found in the porphyritic biotite granites within deep drill cores,

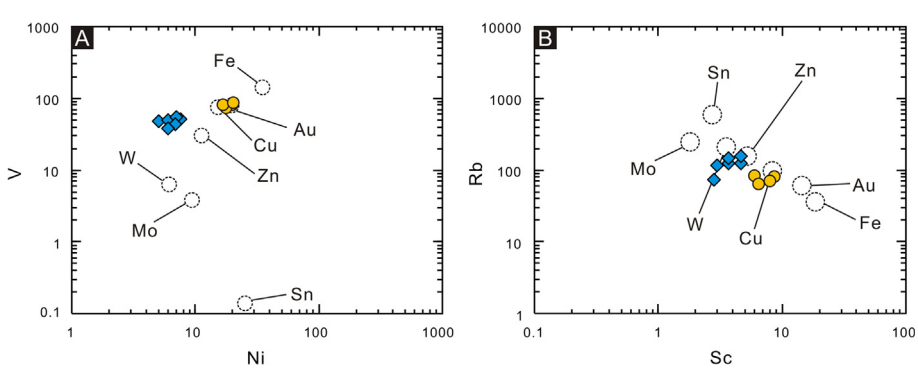

Fig. 12. (A) Ni versus V and. (B) Sc versus Rb correlation diagrams for intrusions associated with Cu mineralization at Baoshan deposit, open circles indicates the average compositions of plutons associated with skarn deposit types worldwide (Meinert, 1995).

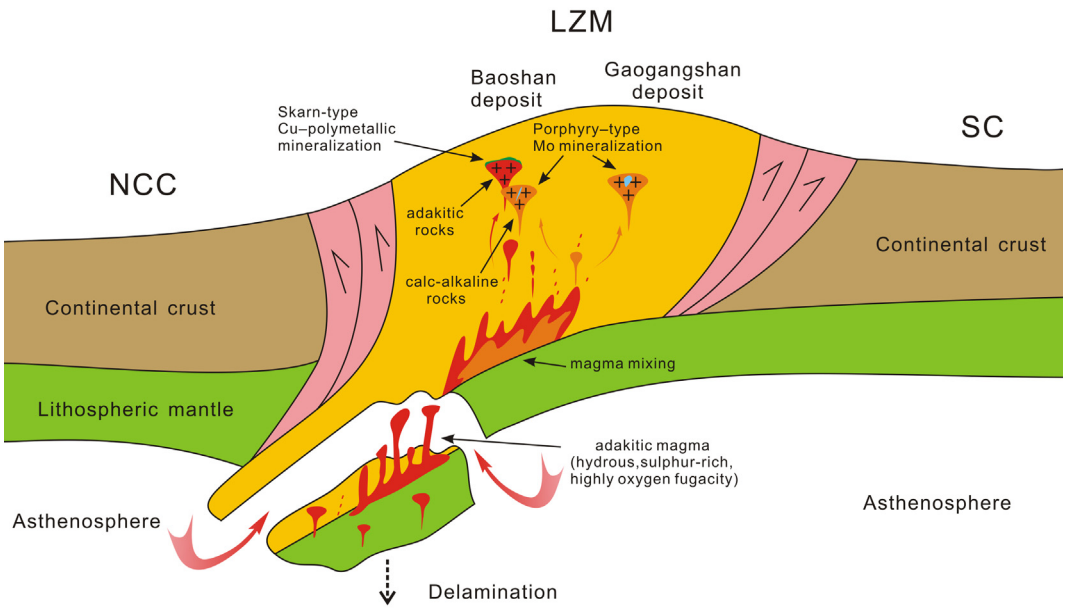

Fig. 13. Sketch showing the genetic model and tectonic setting for the Late Permian–Early Triassic porphyry-skarn mineralizations in the Lesser Xing'an Range. NCC: North China Crton; LZM: Lesser Xing'an Range–Zhangguangcai Range Massif; SC: Siberia craton.

indicating that the Baoshan Cu–polymetallic deposit at depth also has the potential to host porphyry-type ore bodies.

7. Conclusions

Integrating the new zircon U–Pb and molybdenite Re–Os dating, whole-rock geochemistry, and Hf isotopic data presented here, with the results of previous research, leads to the following conclusions:

1. Molybdenite samples yielded a weighted age of 250.3 ± 3.4 Ma, while zircons from the hornblende–quartz monzonite and porphyritic biotite granite yielded U–Pb ages of 252.45 ± 0.70 Ma and 251.10 ± 0.98 Ma, respectively. The zircon U–Pb and molybdenite Re–Os ages are concordant within error limits, indicating that magmatism and mineralization of the Baoshan Cu–polymetallic deposit occurred during the Late Permian–Early Triassic.

2. The geochemical and isotopic data from the Baoshan intrusions imply that the primary magma of the hornblende–quartz monzonite was derived from the partial melting of delaminated lower crust, and that adakitic magma may have reacted with surrounding mantle peridotites during ascent. The primary magma of the porphyritic biotite granite likely originated from magma mixing, comprising both adakitic magmas and ancient crustal materials.

3. Based on the regional geological history, new geochemical and isotopic data for the intrusions, we suggest that mineralization of the Baoshan Cu–polymetallic deposit likely took place in a transitional tectonic setting from collisional orogeny to extension, after collision of the North China Plate and Songnen Block, during the latter stages of the Xingmeng orogeny.

4. Ore-forming materials were mainly derived from adakitic magmas with high oxygen fugacity, which incorporated significant amounts of ore-forming elements.

Acknowledgments

This research was supported by the Program for National Natural Science Foundation of China (Grant No. 41390444; 41172072), and Program of the China Geological Survey (Grant No. 12120114028201). We sincerely thank the staff of Key Laboratory of Orogenic Belts and Crustal Evolution, Ministry of Education, Peking University for assistance with the zircon U–Pb dating, as well as the State Key Laboratory for Mineral Deposits Research, Nanjing University for help in zircon Hf isotopic analyses. Fieldwork was supported by Heilongjiang Bureau of Geological Exploration for Nonferrous Metals.

References

Andersen, T., 2002. Correction of common lead in U-Pb analyses that do not report 204Pb. Chem. Geol. 192 (1–2), 59–79.
Barbarin, B., 1999. A review of the relationships between granitoid types, their origins and their geodynamic environments. Lithos 46, 605–626.
Bergantz, G.W., 1989. Underplating and partial melting: implications for melt generation and extraction. Science 245 (4922), 1093–1095.
Blichert-Toft, J., Albarède, F., 1997. The Lu–Hf geochemistry of chondrites and the evolution of the mantle–crust system. Earth Planet. Sci. Lett. 148 (1–2), 243–258.
Boynton, W.V., 1984. Geochemistry of the rare earth elements, meteorite studies. In: Henderson, P. (Ed.), Rare Earth Element Geochemistry. Elsevier, pp. 63–114.
Cao, H.H., Xu, W.L., Pei, F.P., Wang, Z.W., Wang, F., Wang, Z.J., 2013. Zircon U-Pb geochronology and petrogenesis of the Late Paleozoic-Early Mesozoic intrusive rocks in the eastern segment of the northern margin of the North China Block. Lithos 170–171, 191–207.
Chappell, B.W., White, A.J.R., 1992. I–type and S–type granites in the Lachlan Fold Belt. Transactions of the Royal Society of Edinburgh. Earth Sci. 83 (1–2), 1–26.
Chappell, B.W., White, A.J.R., 2001. Two contrasting granite types: 25 years later. Aust. J. Earth Sci. 48 (4), 489–499.
Chen, B., Jahn, B.M., Tian, W., 2009. Evolution of the Solonker suture zone: constraints from zircon U-Pb ages, Hf isotopic ratios and whole–rock Nd–Sr isotope compositions of subduction and collision-related magmas and forearc sediments. J. Asian Earth Sci. 34, 245–257.
Chen, J., Sun, F.Y., Pan, T., Wang, J., Huo, L., 2012. Geological features of Huojihe molybdenum deposit in Heilongjiang, and geochronology and geochemistry of mineralized granodiorite. J. Jilin Univ. (Earth Sci. Ed.) 42, 207–215 (in Chinese with English abstract).
Chen, Y.J., Sun, J.G., Ren, L., Zhang, Y., Men, L.J., 2013. Petrogenesis of the Wudaogou intermediate-mafic complex, NW China: zircon U-Pb dating, whole-rock and isotope geochemistry, and geological implications. Int. Geol. Rev. 55 (16), 1959–1977.
Cui, P.L., Sun, J.G., Han, S.J., Zhang, P., Zhang, Y., Bai, L.A., Gu, A.L., 2013. Zircon U-Pb–Hf isotopes and bulk–rock geochemistry of gneissic granites in the northern Jiamusi Massif, Central Asian Orogenic Belt: implications for Middle Permian collisional orogeny and Mesoproterozoic crustal evolution. Int. Geol. Rev. 55 (9), 1109–1125.

Defant, M.J., Drummond, M.S., 1990. Derivation of some modern arc magmas by melting of young subducted lithosphere. Nature 347, 662–665.
Defant, M.J., Kepezhinskas, P., 2001. Evidence suggests slab melting in arc magmas. Eos Trans. AGU. 82 (6), 65–69.
Defant, M.J., Xu, J.F., Kepezhinskas, P., Wang, Q., Zhang, Q., Xiao, L., 2002. Adakites: some Variations on a theme. Acta Petrol. Sin. 18 (2), 129–142.
Du, X.H., Zhang, Y., 2015. Metallogenic geochronology and geochemical characteristics of Huojihe molybdenum deposit in the Heilongjiang Province. Resources Industries 17 (1), 1–8 (in Chinese with English abstract).
Du, A.D., Wu, S.Q., Sun, D.Z., Wang, S.X., Qu, W.J., Markey, R., Stain, H., Morgan, J., Malinovskiy, D., 2004. Preparation and certification of Re–Os dating reference materials: molybdenites HLP and JDC. Geostand. Geoanal. Res. 28 (1), 41–52.
Eby, G.N., Woolley, A.R., Din, V., Platt, G., 1998. Geochemistry and petrogenesis of nepheline syenite. Kasungu-Chipala, Ilomba, and Ulindi nepheline syenite intrusions, North Nyasa Alkaline Province, Malawi. J. Petrol. 39 (8), 1405–1424.
Gao, S., Liu, X.M., Yuan, H.L., Hattendorf, B., Gunther, D., Chen, L., Hu, S.H., 2002. Determination of forty two major and trace elements in USGS and NIST SRM glasses by laser ablation–inductively coupled plasma–mass spectrometry. Geostand. Geoanal. Res. 26 (2), 181–196.
Gao, S., Rudnick, R.L., Yuan, H.L., Liu, X.M., Liu, Y.S., Xu, W.L., Ling, W.L., Ayers, J., Wang, X.C., Wang, Q.H., 2004. Recycling lower continental crust in the North China craton. Nature 432 (7019), 892–897.
Griffin, W.L., Pearson, N.J., Belousova, E., Jackson, S.E., Van Achterbergh, E., O.Reilly, S.Y., Shee, S.R., 2000. The Hf isotope composition of cratonic mantle, LAM–MC–ICPMS analysis of zircon megacrysts in kimberlites. Geochim. Cosmochim. Acta 64 (1), 133–147.
Griffin, W.L., Wang, X., Jackson, S.E., Pearson, N.J., O'Reilly, S.Y., Xu, X.S., Zhou, X.M., 2002. Zircon chemistry and magma genesis, SE China: in-situ analysis of Hf isotopes, Tonglu and Pingtan igneous complexes. Lithos 61 (3), 237–269.
Guan, Q., Zhu, D.C., Zhao, Z.D., Dong, G.C., Zhang, L.L., Li, X.W., Liu, M., Mo, X.X., Liu, Y.S., Yuan, H.L., 2011. Crustal thickening prior to 38 Ma in southern Tibet: evidence from lower crust-derived adakitic magmatism in the Gangdese Batholith. Gondwana Res. 21, 88–89.
Han, Z.X., Hao, Z.P., Hou, M., 1995. Metallogenic series of ore deposits related to Caledonian Granitoids in Xiaohingganling region. Mineral Deposits 14 (4), 293–302 (in Chinese with English abstract).
Hao, Y.J., Ren, Y.S., Zhao, H.L., Zou, X.T., Chen, C., Hou, Z.S., Qu, W.J., 2013. Re–Os isotopic dating of the molybdenite from the Cuihongshan W-Mo polymetallic deposit in Heilongjiang Province and its geological significance. J. Jilin Univ. (Earth Sci. Ed.) 43 (6), 1840–1850 (in Chinese with English abstract).
Hao, Y.J., Ren, Y.S., Yang, Q., Duan, M.X., Sun, Q., Fu, L.C., Li, C., 2015. Ore genesis and formation age of the Gaogangshan Mo deposit, Heilongjiang Province, NE China. Resour. Geol. 65 (2), 177–192.
Hao, B.W., Deng, J., Bagas, L., Ge, L.S., Nie, F.J., Turner, S., Qing, M., 2016. The Gaosongshan epithermal gold deposit in the Lesser Hinggan Range of the Heilongjiang Province, NE China: implications for Early Cretaceous mineralization. Ore Geol. Rev. 73, 179–197.
HBGMR (Heilongjiang Bureau of Geology and Mineral Resources), 1993. Regional Geology of Heilongjiang Province. Geological Publishing House, Beijing, pp. 1-418 (in Chinese with English abstract).
Hoskin, P.W.O., Schaltegger, U., 2003. The composition of zircon and igneous and metamorphic petrogenesis. Rev. Mineral. Geochem. 53 (1), 27–62.
Hou, K.J., Li, Y.H., Zou, T.R., Qu, X.M., Shi, Y.R., Xie, G.Q., 2007. Laser ablation–MC–ICP–MS technique for Hf isotope microanalysis of zircon and its geological applications. Acta Petrol. Sin. 23 (10), 2595–2604 (in Chinese with English abstract).
Hu, X.L., Ding, Z.J., He, M.C., Yao, S.Z., Zhu, B.P., Shen, J., Chen, B., 2014a. A porphyry–skarn metallogenic system in the Lesser Xing'an Range, NE China: implications from U-Pb and Re–Os geochronology and Sr–Nd–Hf isotopes of the Luming Mo and Xulaojiugou Pb–Zn deposits. J. Asian Earth Sci. 90, 88–100.
Hu, X.L., Ding, Z.J., He, M.C., Yao, S.Z., Zhu, B.P., Shen, J., Chen, B., 2014b. Two epochs of magmatism and metallogeny in the Cuihongshan Fe–polymetallic deposit, Heilongjiang Province, NE China: constrains from U-Pb and Re–Os geochronology and Lu–Hf isotopes. J. Geochem. Explor. 143 (3), 116–126.
Iizuka, T., Hirata, T., 2005. Improvements of precision and accuracy in in situ Hf isotopemicroanalysis of zircon using the laser ablation-MC-ICPMS technique. Chem. Geol. 220 (1–2), 121–137.
Irvine, T.N., Baragar, W.R.A., 1971. A guide to the chemical classification of the common volcanic rocks. Can. J. Earth Sci. 8 (5), 523–548.
Isozaki, Y., 1997. Jurassic accretion tectonics of Japan. Isl. Arc 6 (1), 25–51.
Jahn, B.M., Wu, F.Y., Chen, B., 2000. Granitoids of the Central Asian Orogenic Belt and continental growth in the Phanerozoic. Earth Environ. Sci. Tr. Soc. 91 (1–2), 181–193.
Jahn, B.M., Capdevila, R., Liu, D.Y., Vernon, A., Badarch, G., 2004. Sources of Phanerozoic granitoids in the transect Bayanhongor-Ulaan Baatar, Mongolia: geochemical and Nd isotopic evidence, and implications for Phanerozoic crustal growth. J. Asian Earth Sci. 23 (5), 629–653.
Kay, R.W., Kay, S.M., 1993. Delamination and delamination magmatism. Tectonophysics 219 (1–3), 177–189.
Kepezhinskas, P.K., Defant, M.J., Drummond, M.S., 1995. Na metasomatism in the island-arc mantle by slab melt-peridotite interaction: evidence from mantle interaction: Evidence from mantle xenoliths in the north Kamchatka arc. J. Petrol. 36 (6), 1505–1527.
Koschek, G., 1993. Origin and significance of the SEM Cathodoluminescence from zircon. J. Microsc 171 (3), 223–232.
Li, C.N., 1992. Igneous Petrology of Trace Elements. China University of Geosciences Press, Wuhan, pp. 1–195 (in Chinese).
Li, J.Y., 2006. Permian geodynamic setting of Northeast China and adjacent regions: closure of the Paleo-Asian Ocean and subduction of the Paleo-Pacific Plate. J. Asian Earth Sci. 26 (3), 207–224.
Li, X.H., Li, Z.X., Li, W.X., Liu, Y., Yuan, C., Wei, G.J., Qi, C.S., 2007. U-Pb zircon, geochemical and Sr–Nd–Hf isotopic constraints on age and origin of Jurassic I– and A–type granites from central Guangdong, SE China: a major igneous event in response to foundering of a subducted flat–slab? Lithos 96 (1–2), 186–204.
Liang, B.S., 2014. Geological characteristics and genesis of iron polymetallic orefield in Ergu area, Heilongjiang Province (Master Degree Thesis). Jilin University, Changchun, pp. 1–65 (in Chinese with English abstract).
Lightfoot, P.C., Hawkesworth, C.J., Sethna, S.F., 1987. Petrogenesis of rhyolites and trachytes from the Deccan Trap: Sr, Nd and Pb isotope and trace element evidence. Contrib. Mineral. Petr. 95 (1), 44–54.
Liu, J.M., Zhang, R., Zhang, Q.Z., 2004. The regional metallogeny of Da Hinggan Ling. China. Earth Sci. Front. 11 (1), 269–277 (in Chinese with English abstract).
Liu, J.F., Chi, X.G., Dong, C.Y., Zhao, Z., Li, G.R., Zhao, Y.D., 2008. Discovery of Early Paleozoic granites in the eastern Xiao Hinggan Mountains, northeastern China and their tectonic significance. Geol. Bull. China 27 (4), 534–544 (in Chinese with English abstract).
Liu, Y.J., Zhang, X.Z., Jin, W., Chi, X.G., Wang, C.W., Ma, Z.H., Han, G.Q., Wen, Q.B., Li, W., Wang, W.D., Zhao, X.F., 2010. Late Paleozoic tectonic evolution in Northeast China. Geol. China 37 (4), 943–951 (in Chinese with English abstract).
Liu, C.Y., Deng, J.F., Luo, Z.H., Tian, S.P., Zhang, Y., Zhong, C.T., Selby, D., Zhao, H.D., 2014. Post–batholith metallogenesis: evidence from Luming super large molybdenite deposit in Lesser Xing'an Range. Acta Petrol. Sin. 30 (11), 3400–3418 (in Chinese with English abstract).
Liu, R.P., Gu, X.X., Zhang, Y.M., Wang, J.L., Zheng, L., Gao, H.J., 2015. Zircon U-Pb geochronology and petrogeochemistry of host igneous rocks of the Dong'an gold deposit in Heilongjiang Province. NE China. Acta Petrol. Sin. 31 (5), 1391–1408 (in Chinese with English abstract).
Ludwig, K.R., 2003. Isoplot 3.0, a geochronological toolkit for Microsoft Excel. Berkeley Geochronology Center. Spec. Publ. 4, 1–71.
Ma, S.Q., Chen, J., 2012. Geochronology and geochemistry of granite of the Luming molybdenum deposit in Heilongjiang and their geological significance. Geol. China 39 (5), 1162–1171 (in Chinese with English abstract).
Maniar, P.D., Piccoli, P.M., 1989. Tectonic discrimination of granitoids. Geol. Soc. Am. Bull. 101 (5), 635–643.
Martin, H., Smithies, R.H., Rapp, R., Moyen, J.F., Champion, D., 2005. An overview of adakite, tonalite– trondhjemite– granodiorite (TTG), and sanukitoid: relationships and some implications for crustal evolution. Lithos 79 (1–2), 1–24.
Meinert, L.D., 1995. Compositional variation of igneous rocks associated with skarn deposits–chemical evidence for a genetic connection between petrogenesis and mineralization. Mineralogical Association of Canada Short Course Series 23, 401–418.
Middlemost, E.A.K., 1972. A simple classification of volcanic rocks. Bull. volcanol. 36 (2), 382–397.
Middlemost, E.A.K., 1994. Naming materials in the magma/igneous rock system. Earth Sci. Rev. 37 (3–4), 215–224.
Mungall, J.E., 2002. Roasting the mantle: Slab melting and the genesis of major Au and Au–rich Cu deposits. Geology 30 (10), 915–918.
Nowell, G.M., Kempton, P.D., Noble, S.R., Fitton, J.G., Saunders, A.D., Mahoney, J.J., Taylor, R.N., 1998. High precision Hf isotope measurements of MORB and OIB by thermal ionisation mass spectrometry: insights into the depleted mantle. Chem. Geol. 149 (3–4), 211–233.
Otamendi, J.E., De La Rosa, J.D., Patiño Douce, A.E., Castro, A., 2002. Rayleigh fractionation of heavy rare earths and yttrium during metamorphic garnet growth. Geology 30 (2), 159–162.
Oyarzun, R., Márquez, A., Lillo, J., López, I., Rivera, S., 2001. Giant versus small porphyry copper deposits of Cenozoic age in northern Chile: adakitic versus normal calc-alkaline magmatism. Miner. Deposita 36 (8), 794–798.
Patiño Douce, A.E., Harris, N., 1998. Experimental constraints on Himalayan anatexis. J. Petrol. 39 (4), 689–710.
Patiño Douce, A.E., Mccarthy, T.C., 1998. Melting of crustal rocks during continental collision and subduction. In: Hacker, B.R., Liu, J.G. (Eds.), When Continents Collide: Geodynamics of Ultrahigh Pressure Rocks. Kluwer Academic Publisher, Netherlands, pp. 27–55.
Pearce, J.A., Harris, N.B.W., Tindle, A.G., 1984. Trace element discrimination diagrams for the tectonic interpretation of granitic rocks. J. Petrol. 25, 956–983.
Peccerillo, A., Taylor, S.R., 1976. Geochemistry of eocene calc–alkaline volcanic rocks from the Kastamonu area, Northern Turkey. Contrib. Mineral. Petr. 58 (1), 63–81.
Rapp, R.P., Watson, E.B., 1995. Dehydration melting of metabasalt at 8–32 kbar: implications for continental growth and crust–mantle recycling. J. Petrol. 36 (4), 891–931.
Rapp, R.P., Shimizu, N., Norman, M.D., Applegate, G.S., 1999. Reaction between slab–derived melts and peridotite in the mantle wedge: Experimental constraints at 3.8 GPa. Chem. Geol. 160 (4), 335–356.
Ren, J.S., Niu, B.G., Liu, Z.G., 1999. Soft collision, superposition orogeny and polycyclic suturing. Earth Sci. Front. 6 (3), 85–93 (in Chinese with English abstract).
Ren, L., Sun, J.G., Tang, C., Men, L.J., Li, Y.X., Cui, P.L., 2015. Petrogenic and metallogenic geochronology and its geological implications of Lianzhushan gold deposit, Jiayin, Heilongjiang Province. Acta Petrol. Sin. 31 (8), 2435–2449 (in Chinese with English abstract).

Sajona, F.G., Maury, R.C., 1998. Association of adakites with gold and copper mineralization in the Philippines. Comptes Rendus De L'académie Des Sciences-Series IIA–Earth and Planetary. Science 326 (1), 27–34.
Scedilengör, A.M.C., Natal'in, B.A., Burtman, V.S., 1993. Evolution of the Altaid tectonic collage and Palaeozoic crustal growth in Eurasia. Nature 364, 299–307.
Scherer, E., Munker, C., Mezger, K., 2001. Calibration of the Lutetium-Hafnium clock. Science 293 (5530), 683–687.
Schiano, P., Monzier, M., Eissen, J.P., Martin, H., Koga, K.T., 2010. Simple mixing as the major control of the evolution of volcanic suites in the Ecuadorian Andes. Contrib. Mineral. Petr. 160 (2), 297–312.
Shao, J.A., Tang, K.D., 1995. Terranes in Northeast China and Evolution of Northeast Asia continental margin. Earthquake Press, Beijing, pp. 1–185 (in Chinese).
Shao, J., Li, X.R., Yang, H.Z., 2011. Zircon SHRIMP U-Pb dating of granite in the Cuihongshan polymetallic deposit and its geological implications. Acta Geosci. Sin. 32 (2), 163–170 (in Chinese with English abstract).
Shirey, S.B., Walker, R.J., 1995. Carius tube digestion for low–blank rhenium–osmium analysis. Anal. Chem. 67 (13), 2136–2141.
Smithies, R.H., 2000. The Archaean tonalite–trondhjemite–granodiorite (TTG) series is not an analogue of Cenozoic adakite. Earth Planet. Sci. Lett. 182 (1), 115–125.
Smoliar, M.I., Walker, R.J., Morgan, J.W., 1996. Re–Os ages of group IIA, IIIA, IVA, and IVB iron meteorites. Science 271 (5252), 1099–1102.
Stein, H.J., Markey, R.J., Morgan, J.W., Du, A., Sun, Y., 1997. Highly precise and accurate Re–Os ages for molybdenite from the East Qinling molybdenum belt, Shaanxi Province, China. Econ. Geol. 92 (7), 827–835.
Sun, S.S., Mcdonough, W.F., 1989. Chemical and isotopic systematics of oceanic basalts: implications for mantle composition and processes. In: Saunders, A.D., Norry, M.J. (Eds.), Magmatism in the Ocean Basins. Geol. Soc. Spec. Publ., London 42, pp. 313–345.
Sun, Y.L., Zhou, M.F., Sun, M., 2001. Routine Os analysis by isotope dilution–inductively coupled plasma mass spectrometry: OsO_4 in water solution gives high sensitivity. J. Anal. Atom. Spectrom. 16 (4), 345–349.
Sun, D.Y., Wu, F.Y., Gao, S., 2004a. LA-ICP-MS Zircon U-Pb age of the Qingshui pluton in the East Xiao Hinggan Mountains. Acta Geosci. Sin. 25 (2), 213–218 (in Chinese with English abstract).
Sun, D.Y., Wu, F.Y., Zhang, Y.B., Gao, S., 2004b. The final closing time of the West Lamulun River–Changchun–Yanji plate suture zone. Acta Geosci. Sin. 34 (2), 174–181 (in Chinese with English abstract).
Sun, W.D., Arculus, R.J., Kamenetsky, V.S., Binns, R.A., 2004c. Release of gold–bearing fluids in convergent margin magmas prompted by magnetite crystallization. Nature 431 (7011), 975–978.
Sun, Y.L., Xu, P., Li, J., He, K., Chu, Z.Y., Wang, C.Y., 2010. A practical method for determination of molybdenite Re–Os age by inductively coupled plasma–mass spectrometry combined with Carius tube–HNO_3 digestion. Anal. Methods–UK 2 (5), 575–581.
Sun, J.G., Zhang, Y., Han, S.J., Men, L.J., Li, Y.X., Chai, P., Yang, F., 2013a. Timing of formation and geological setting of low–sulphidation epithermal gold deposits in the continental margin of NE China. Int. Geol. Rev. 55 (5), 142–161.
Sun, J.G., Han, S.J., Zhang, Y., Xing, S.W., Bai, L.A., 2013b. Diagenesis and metallogenetic mechanisms of the Tuanjiegou gold deposit from the Lesser Xing'an Range, NE China: zircon U-Pb geochronology and Lu–Hf isotopic constraints. J. Asian Earth Sci. 62, 373–388.
Sun, Q.L., Sun, J.G., Zhao, K.Q., Tang, C., Zhang, Y., Han, S.J., Yang, F., 2014. Re–Os isotopic dating and geological significance of Luming porphyry molybdenum deposit in Heilongjiang. Glob. Geol. 32 (2), 418–425 (in Chinese with English abstract).
Sylvester, P.J., 1998. Post–collisional strongly peraluminous granites. Lithos 45, 29–44.
Tan, H.Y., Shu, G.L., Lv, J.C., Han, R.P., Zhang, S., Kou, L.L., 2012. LA–ICP–MS Zircon U-Pb and molybdenite Re–Os dating for the Luming large-scale molybdenum deposit in Xiao Hinggan Mountains and its geological implication. J. Jilin Univ. (Earth Sci. Ed.) 42, 1757–1770 (in Chinese with English abstract).
Taylor, S.R., Mclennan, S.M., 1985. The Continental Crust: Its Composition and Evolution. Blackwell Scientific Publish, pp. 57–72.
Wang, Q., Xu, J.F., Zhao, Z.H., 2001. The summary and comment on research on a new kind of igneous rock–adakite. Adv. Earth Sci. 16 (2), 201–208 (in Chinese with English abstract).
Wang, Q., Zhao, Z.H., Bao, Z.W., Xu, J.F., Liu, W., Li, C.F., Bai, Z.H., Xiong, X.L., 2004. Geochemistry and petrogenesis of the Tongshankou and Yinzu adakitic intrusive rocks and the associated porphyry copper–molybdenum mineralization in Southeast Hubei, East China. Resour. Geol. 54 (2), 137–152.
Wang, Q., Xu, J.F., Jian, P., Bao, Z.W., Zhao, Z.H., Li, C.F., Xiong, X.L., Ma, J.L., 2006. Petrogenesis of adakitic porphyries in an extensional tectonic setting, Dexing, South China: implications for the genesis of porphyry copper mineralization. J. Petrol. 47 (1), 119–144.
Wang, Q., Wyman, D.A., Xu, J.F., Zhao, Z.H., Jian, P., Zi, F., 2007. Partial melting of thickened or delaminated lower crust in the middle of Eastern China: implications for Cu–Au mineralization. J. Geol. 115 (2), 149–161.
Wang, F., Xu, W.L., Meng, E., Gao, F.H., Zhang, H.H., Pei, F.P., Zhao, L., Yang, Y., 2014. Precambrian terrane within the Songnen-Zhangguangcai Range Massif, NE China: evidence from U-Pb ages of detrital zircons from the Dongfengshan and Tadong groups. Gondwana Res. 26 (1), 402–413.
Wang, Z.W., Xu, W.L., Pei, F.P., Wang, F., Guo, P., 2016. Geochronology and geochemistry of early Paleozoic igneous rocks of the Lesser Xing'an Range, NE China: implications for the tectonic evolution of the eastern Central Asian Orogenic Belt. Lithos 261, 144–163.
Wei, H.Y., 2012. The Geochronology and Petrogenesis of Granite in Yichun-Hegang Area, Heilongjiang Province (Master Degree Thesis). Jilin University, Changchun (in Chinese with English abstract).
Whalen, J.B., Currie, K.L., Chappell, B.W., 1987. A–type granites: geochemical characteristics, discrimination and petrogenesis. Contrib. Mineral. Petr. 95 (4), 407–419.
Windley, B.F., Alexeiev, D., Xiao, W.J., Kröner, A., Badarch, G., 2007. Tectonic models for accretion of the Central Asian Orogenic Belt. J. Geol. Soc. London 164 (12), 31–47.
Woodhead, J.D., Hergt, J.M., 2005. A preliminary appraisal of seven natural zircon reference materials for in situ Hf isotope determination. Geostand. Geoanal. Res. 29 (2), 183–195.
Wu, F.Y., Sun, D.Y., Lin, Q., 1999. Petrogenesis of the Phanerozoic granites and crustal growth in Northeast China. Acta Petrol. Sin. 15 (2), 181–189 (in Chinese with English abstract).
Wu, F.Y., Jahn, B.M., Wilde, S., Sun, D.Y., 2000. Phanerozoic crustal growth. U-Pb and Sr–Nd isotopic evidence from the granites in northeastern China. Tectonophysics 328 (1–2), 89–113.
Wu, F.Y., Sun, D.Y., Jahn, B.M., Wilde, S., 2004. A Jurassic garnet-bearing granitic pluton from NE China showing tetrad REE patterns. J. Asian Earth Sci. 23 (5), 731–744.
Wu, F.Y., Yang, Y.H., Xie, L.W., Yang, J.H., Xu, P., 2006. Hf isotopic compositions of the standard zircons and baddeleyites used in U-Pb geochronology. Chem. Geol. 234 (1–2), 105–126.
Wu, F.Y., Zhao, G.C., Sun, D.Y., Wilde, S.A., Yang, J.H., 2007a. The Hulan Group. its role in the evolution of the Central Asian Orogenic Belt of NE China. J. Asian Earth Sci. 30 (3–4), 542–556.
Wu, F.Y., Yang, J.H., Lo, C.H., Wilde, S.A., Sun, D.Y., Jahn, B.M., 2007b. The Heilongjiang Group: a Jurassic accretionary complexin the Jiamusi Massif at the western Pacific margin of northeastern China. J. Asian Earth Sci. 30, 542–556.
Wu, F.Y., Sun, D.Y., Ge, W.C., Zhang, Y.B., Grant, M.L., Wilde, S.A., Jahn, B.M., 2011. Geochronology of the Phanerozoic granitoids in northeastern China. J. Asian Earth Sci. 41 (1), 1–30.
Wyborn, D., Sun, S.S., 1994. Sulphur–undersaturated magmatism–a key factor for generating magma–related copper–gold deposits. AGSO Research Newsletter 21, 7–8.
Xiao, W.J., Windley, B.F., Hao, J., Zhai, M.G., 2003. Accretion leading to collision and the Permian Solonker suture, Inner Mongolia, China. termination of the central Asian orogenic belt. Tectonics 22 (6), 1069–1089.
Xiao, W.J., Zhang, L.C., Qin, K.Z., Sun, S., Li, J.Y., 2004. Paleozoic accretionary and collisional tectonics of the eastern Tienshan (China): implications for the continental growth of Central Asia. Am. J. Sci. 304, 370–395.
Xiao, W.J., Windley, B.F., Huang, B.C., Han, C.M., Yuan, C., Chen, H.L., Sun, M., Sun, S., Li, J.L., 2009. End-Permian to mid–Triassic termination of the accretionary processes of the southern Altaids: implications for the geodynamic evolution, Phanerozoic continental growth, and metallogeny of Central Asia. Int. J. Earth Sci. 98 (6), 1189–1217.
Xiong, X.L., Zhao, Z.H., Bai, Z.H., Mei, H.J., Xu, J.F., Wang, Q., 2001. Origin of Awulale adakitic sodium-rich rocks in western Tianshan. Constraints for Nd and Sr isotopic compositions. Acta Petrol. Sin. 17 (4), 514–522 (in Chinese with English abstract).
Xiong, X.L., Cai, Z.Y., Niu, H.C., Chen, Y.B., Wang, Q., Zhao, Z.H., Wu, J.H., 2005a. The Late Paleozoic adakites in eastern Tianshan area and their metallogenetic significance. Acta Petrol. Sin. 21 (3), 967–976 (in Chinese with English abstract).
Xiong, X.L., Adam, J., Green, T.H., 2005b. Rutile stability and rutile/melt HFSE partitioning during partial melting of hydrous basalt: implications for TTG genesis. Chem. Geol. 218 (3–4), 339–359.
Xu, J.F., Shinjo, R., Defant, M.J., Wang, Q., Rapp, R.P., 2002. Origin of Mesozoic adakitic intrusive rocks in the Ningzhen area of east China: partial melting of delaminated lower continental crust? Geology 30 (12), 1111–1114.
Xu, W.L., Wang, F., Meng, E., Gao, F.H., Pei, F.P., Yu, J.J., Tang, J., 2012. Paleozoic-Early Mesozoic tectonic evolution in the Eastern Heilongjiang Province, NE China: evidence from igneous rock association and U-Pb geochronology of detrital zircons. J. Jilin Univ. (Earth Sci. Ed.) 42 (5), 1378–1389 (in Chinese with English abstract).
Xu, M.J., Xu, W.L., Wang, F., Gao, F.H., Yu, J.J., 2013. Geochronology and geochemistry of the Early Jurassic granitoids in the central Lesser Xing'an Range, NE China and its tectonic implications. Acta Petrol. Sin. 29 (2), 354–368 (in Chinese with English abstract).
Yang, J.H., Wu, F.Y., Shao, J.A., Wilde, S.A., Xie, L.W., Liu, X.M., 2006. Constraints on the timing of uplift of the Yanshan fold and thrust belt, North China. Earth Planet. Sci. Lett. 246 (3–4), 336–352.
Yang, Y.C., Han, S.J., Sun, D.Y., Guo, J., Zhang, S.J., 2012. Geological and geochemical features and geochronology of porphyry molybdenum deposits in the Lesser Xing'an Range-Zhangguangcai Range metallogenic belt. Acta Petrol. Sin. 28 (2), 379–390 (in Chinese with English abstract).
Yu, J.J., Wang, F., Xu, W.L., Gao, F.H., Pei, F.P., 2012. Early Jurassic mafic magmatism in the Lesser Xing'an–Zhangguangcai Range, NE China, and its tectonic implications: constraints from zircon U-Pb chronology and geochemistry. Lithos 142–143, 256–266.
Yu, J.J., Wang, F., Xu, W.L., Gao, F.H., Tang, J., 2013. Late Permian tectonic evolution at the southeastern margin of the Songnen-Zhangguangcai Range Massif, NE China: constraints from geochronology and geochemistry of granitoids. Gondwana Res. 24 (2), 635–647.

Zhang, Q., Wang, Y., Qian, Q., Yang, J.H., Wang, Y.L., Zhao, T.P., Guo, G.J., 2001. The characteristics and tectonic–metallogenic significances of the adakites in Yanshan period from eastern China. Acta Petrol. Sin. 17 (2), 236–244 (in Chinese with English abstract).

Zhang, X.H., Zhang, H.F., Tang, Y.J., Wilde, S.A., 2008. Geochemistry of Permian bimodal volcanic rocks from central Inner Mongolia, North China. Implication for Tectonic setting and Phanerozoic continental growth in Central Asian Orogenic Belt. Chem. Geol. 249, 262–281.

Zhang, X.H., Wilde, S.A., Zhang, H.F., Tang, Y.J., Zhai, M.G., 2009a. Geochemistry of hornblende gabbros from Sonidzuoqi, Inner Mongolia, North China: implications for magmatism during the final stage of suprasubduction zone ophiolite formation. Int. Geol. Rev. 51 (4), 345–373.

Zhang, Y.M., Zhang, H.F., Liu, W.C., Zhou, Z.G., 2009b. Timing and petrogenesis of the Damiao granodiorite, Siziwangqi, Inner Mongolia. Acta Petrol. Sin. 25 (12), 3165–3181 (in Chinese with English abstract).

Zhang, Z.C., Mao, J.W., Wang, Y.B., Pirajno, F., Liu, J.L., Zhao, Z.D., 2010. Geochemistry and geochronology of the volcanic rocks associated with the Dong'an adularia–sericite epithermal gold deposit, Lesser Hinggan Range, Heilongjiang province, NE China: constraints on the metallogenesis. Ore Geol. Rev. 37 (3–4), 158–174.

Zhang, L.L., Liu, C., Zhou, S., Sun, K., Qiu, R.Z., Feng, Y., 2014. Characteristics of ore–bearing granites and ore–forming age of the Huojihe molybdenum deposit in Lesser Xing'an Range. Acta Petrol. Sin. 30 (11), 3419–3431 (in Chinese with English abstract).

Zhang, Y.M., Gu, X.X., Liu, R.P., Sun, X., Li, X.L., Zheng, L., 2017. Geology, geochronology and geochemistry of the Gaogangshan Mo deposit: a newly discovered Permo-Triassic collision–type Mo mineralization in the Lesser Xing'an Range, NE China. Ore Geol. Rev. 81, 672–688.

Zhao, Z.H., 1997. Principle of Trace Elements Geochemistry. Science Press, Beijing, pp. 71–73 (in Chinese).

Zhao, H.D., 2009. Paleozoic Igneous Rock Assemblages and Tectonic Evolution in Southern Xiaoxing'anling– northern Zhangguangcailing in Northeastern China (Doctor Degree Thesis). China University of Geosciences, Beijing (in Chinese with English abstract).

Zhao, Y., Yang, Z.Y., Ma, X.H., 1994. Geotectonic transition from paleoasian system and paleotethyan system to paleopacific active continental margin in Eastern Asia. Sci. Geol. Sin. 29 (2), 105–119 (in Chinese with English abstract).

Zhao, Z.H., Wang, Q., Xiong, L.G., Zhang, H.X., Niu, H.C., Xu, J.F., Bai, Z.H., Qiao, Y.L., 2006. Two types of adakites in North Xinjiang, China. Acta Petrol. Sin. 22 (5), 1249–1265 (in Chinese with English abstract).

Zhou, J.B., Wilde, S.A., Zhang, X.Z., Zhao, G.C., Zheng, C.Q., Wang, Y.J., Zhang, X.H., 2009. The onset of Pacific margin accretion in NE China: evidence from the Heilongjiang high–pressure metamorphic belt. Tectonophysics 478 (3), 230–246.

Zhou, J.B., Zhang, X.Z., Wilde, S.A., Zheng, C.Q., 2011a. Confirming of the Heilongjiang ~500Ma pan–African khondalite belt and its tectonic implications. Acta Petrol. Sin. 27 (4), 1235–1245 (in Chinese with English abstract).

Zhou, J.B., Wilde, S.A., Zhang, X.Z., Zhao, G.C., Liu, F.L., Qiao, D.W., Ren, S.M., Liu, J.H., 2011b. A >1300 km late pan–African metamorphic belt in NE China: new evidence from the Xing'an Block and its tectonic implications. Tectonophysics 509 (3), 280–292.

Zhu, D.C., Mo, X.X., Wang, L.Q., Zhao, Z.D., Niu, Y.L., Zhou, C.Y., Yang, Y.H., 2009. Petrogenesis of highly fractionated I–type granites in the Zayu area of eastern Gangdese, Tibet: constraints from zircon U-Pb geochronology, geochemistry and Sr–Nd–Hf isotopes. Sci. China (Series D) 52, 1223–1239.